LA-UR-17-28837

Title: Neutron Characterization of Encapsulated ATF-1/LANL-1 Mockup Fuel Capsules

Author(s): Vogel, Sven C.
Borges, Nicholas Paul
Losko, Adrian Simon
Mosby, Shea Morgan
Voit, Stewart Lancaster
White, Joshua Taylor
Byler, Darrin David
Dunwoody, John Tyler
Nelson, Andrew Thomas
Mcclellan, Kenneth James

Intended for: Report

Issued: 2017-09-28

Neutron Characterization of Encapsulated ATF-1/LANL-1 Mockup Fuel Capsules

Nuclear Technology Research and Development

S. C. Vogel,
N. P. Borges[1], A. S. Losko,
S. Mosby, S. Voit, J. White, D.
Byler, J. Dunwoody, A. Nelson,
K. J. McClellan,
LANL, [1]Worcester Polytechnical Institute

SUMMARY

Twenty pellets of mock-up accident tolerant fuels UN-U_3Si_5 were produced at LANL and loaded in two rodlet/capsule assemblies. Tomographic imaging and diffraction measurements were performed to characterize these samples at the Flight-Path 5 and HIPPO beam lines at LANSCE/LANL between November 2016 and January 2017 as well as in August 2017. The entire ~10 cm long, ~1 cm diameter fuel volume could be characterized, however due to time constraints only 2 mm slices in 4mm increments were characterized with neutron diffraction and a 28mm subset of the entire sample was characterized with energy-resolved neutron imaging. The double encapsulation of the fuel into two steel containers does not pose a problem for the neutron analysis and the methods could be applied to enriched (demonstrated previously, e.g. [11]) as well irradiated fuels.

Both approaches, imaging and diffraction, indicate that the fuel pellets are homogeneous. Minor deviations from the homogeneity were observed in the U_3Si_5 by diffraction. The observed changes are consistent with melting and resolidification of larger volumes of U_3Si_5 (texture) which may absorb some UN, leading to lattice parameter changes.

The goal of the Advanced Non-destructive Fuel Examination work package is the development and application of non-destructive neutron imaging and scattering techniques to ceramic and metallic nuclear fuels. Samples were delivered to LANSCE in November 2016 and data were collected in the LANSCE run cycles that started in September 2016 and ended in February 2017 as well as the run cycle that started in July 2017 and is scheduled to end in December 2017. Due to the unexpected problems with the LANSCE accelerator, data collection in the second run cycle could not start until late August 2017, just in time for this report. Data analysis for some datasets is therefore not fully completed.

Key results include:

- 3D characterization of flaws and isotopic distributions are determined non-destructively in complete rodlets to high spatial resolution. Current improvements in resolution *via* pixel centroiding can provide spatial resolution up to 22 μm, compared to ~100 μm without data processing.

- Detailed analysis of the transmission data and known neutron absorption cross sections allow for interpretation of neutron transmission data. Analysis can provide partial densities for isotopes averaged over the sample or at specific locations. New deployment of liquid scintillator detector allows for high efficiency resonance analysis up to keV neutrons.

- Diffraction data for the analysis of crystallographic phase, lattice parameters, and texture were collected by probing 2mm slices of the capsule, thus allowing spatially resolved measurements of these parameters. While the UN phase is homogeneous, some slight variations were found in the U_3Si_5 phase.

CONTENTS

FIGURES

TABLES

ACRONYMS

AECL	Atomic Energy of Canada Limited
APS	Advanced Photon Source
AFC	Advanced Fuel Cycle
ANDE	Advanced Non-destructive Examination
ASTM	American Society of Testing Materials
ATF	Accident Tolerant Fuel
ATR	Advanced Test Reactor
BWR	Boiling Water Reactor
CCD	Charge-Coupled Device
CEA	French Alternative Energies and Atomic Energy Commission
CT	Computed Tomography
DOE	Department of Energy
DOE/NE	Department of Energy/Nuclear Energy program
DOT	Department of Transportation
EBS	Ethylene bis-stearate
ENDF	Evaluated Nuclear Data File
EPMA	Electron Probe Microanalysis
FCCI	Fuel Cladding Chemical Interaction
FCMI	Fuel Cladding Mechanical Interaction
FCRD	Fuel Cycle Research and Development
FOV	Field of View
FP5	Flight-path 5 (imaging beam line at LANSCE)
FR	Fast Reactor
HEU	Highly Enriched Uranium
HFEF	Hot Fuels Examination Facility
HI	High Intensity
HIPPO	High Pressure/Preferred Orientation neutron diffractometer
IAEA	International Atomic Energy Agency
ICP-MS	Inductively coupled plasma mass spectrometry
IMCL	Irradiated Materials Characterization Laboratory
INL	Idaho National Laboratory
JAEA	Japan Atomic Energy Agency
LANL	Los Alamos National Laboratory

LANSCE	Los Alamos Neutron Science Center
LEU	Low enriched uranium
Linac	Linear Accelerator
LWR	Light Water Reactor
MA	Minor Actinides
MAMOX	Minor Actinide bearing Mixed Oxide Fuels
MCP	Multi-channel plate
MOX	Mixed Oxide Fuels
NDE	Non-Destructive Evaluation
ND-PIE	Non-Destructive Post Irradiation Examination
NNDC	National Nuclear Data Center (at Brookhaven National Laboratory)
NPDF	Neutron Powder Diffractometer/Neutron Pair Distribution Function
NRC	Nuclear Regulatory Commission
NRC	National Research Council Canada
NRTA	Neutron Resonance Transmission Analysis
NSLS	National Synchrotron Light Source
ORNL	Oak Ridge National Laboratory
O/M	Oxygen-to-Metal ratio
PCMI	Pellet Cladding Mechanical Interaction
PIE	Post Irradiation Examination
pRAD	Proton Radiography
PSI	Paul Scherrer Institute
PWR	Pressurized Water Reactor
RE	Rare Earth element
ROI	Region of Interest
SEM	Scanning Electron Microscopy
SMARTS	Spectrometer for Materials Research at Temperature and Stress
TFRE	Transmutation Fuel with Rare earth inclusions
TMRS	Target-Moderator-Reflector System
TEM	Transmission Electron Microscopy
TOF	Time-of-flight
UN	Uranium nitride
U-Si	Uranium silicide (unspecified stoichiometry)
US	United States

NEUTRON CHARACTERIZATION OF ATF-1/LANL MOCKUP FUEL CAPSULES

1.   Introduction

1.1   Science-based Approach to Nuclear Fuel Development

A key enabler for a "science based approach" for accelerated development and certification of new, accident tolerant nuclear fuels is an early and efficient understanding of material behavior at multiple length scales. For new fuel formulations, there is a dearth of irradiation testing experience. When representative irradiation tests take years, it is important to extract the maximum insight possible from each test. Post irradiation examination (PIE) of fuels is mature and sophisticated but measurements in hot cells are expensive and typically examine small volumes of irradiated fuels relying on a limited amount of knowledge of the bulk characteristics of the specimen to select the volume examined destructively. This leaves the possibility that key failure-inducing phenomena will not be observed because of limited PIE. For these reasons, there is value in techniques that can quickly and non-destructively characterize properties over volumes consistent with standard fuel geometries. Applying such methods pre- and post-irradiation unambiguously determines the changes induced by irradiation. Such techniques can inform models on the initial condition of samples and complement, guide, and leverage destructive post irradiation examination. For example, three dimensional characterization of complete fuel pellets within cladding after irradiation could identify regions that are representative of average and atypical response with parameters not accessible by presently applied techniques such as visual inspection, thermal neutron radiography, or acoustic methods.

Typical in-pile irradiation tests of new fuel types last months or years. Demands on PIE may also impose a delay of years before individual samples can be studied. The resulting levels of radioactivity even for rodlets containing just a handful of pellets or metallic fuels of less than a cm^3 in volume require hot cells and remote manipulators to perform destructive PIE. The complexity and cost of such operations limit the PIE possible, thus, there is a premium on knowing where to measure by identifying regions of interest by as many non-destructive characterizations as possible. This research is focused on developing techniques for non-destructive examination of the bulk volume of rodlets containing multiple pellets or metallic fuels of similar dimensions as well as applying these techniques to pre-irradiation characterization.

The first step in this project is to "benchmark" the initial condition of candidate materials before irradiation. The second step will be to make comparable measurements on irradiated rodlets prior to their destructive examination in INL hot cells.   Neutron, proton and (synchrotron) X-ray radiography/tomography techniques all pose opportunities for this endeavor. By virtue of their stand-off capability and ability to probe materials despite an intense gamma field, neutrons and protons both offer potential for study of highly radioactive materials. At Los Alamos neutron based techniques are routinely used to evaluate microstructure, phase and composition for a wide range of materials problems and protons are widely used for dynamic radiography.

The programmatic emphases for developing advanced non-destructive evaluation (ANDE) techniques applicable to irradiated materials are two-fold. First, it will be possible to evaluate fuel materials to guide the destructive post-irradiation examination towards regions of interest that are not obvious with conventional techniques. This will help develop the statistical insight necessary to complement modeling and simulation data. Adding ANDE insight to the standard optical, thermal neutron and gamma ray insights will help identify regions where destructive examination can be focused. This will increase the return from PIE since regions of atypical irradiation performance are more likely to be discovered. A

second reason for ANDE lies in the desire to generate data as soon as possible after removal of the test samples from the reactor. This is a key requirement in accelerating the development and time to licensing of new fuel forms. The philosophy is consistent with improving diagnostics to offer faster turnaround and getting "more out of less". Programmatically, the capabilities under development sets the stage for routine pre-irradiation fuel evaluation and potentially for post-irradiation evaluations of Accident Tolerant Fuels (ATF) or transmutation fuels.

The techniques employed at LANSCE use the pulsed neutron source at the Lujan Center. They rely on co-location with the 800MeV proton accelerator. However, advances in laser based neutron sources with small-scale accelerators for neutron generation (by D-D fusion) or laser-driven pulsed neutron sources [1,2] pose interesting opportunities [3]. Although such small scale sources are not currently capable of neutron production for measurements of the type described here, technological advance is ongoing. It is possible that, in the next decade, a "small-scale" accelerator source with sufficient neutron production performance might become available to provide "pool side" implementation of the techniques described in this report.

1.2   Scope and Goals of this activity

In the current work accident tolerant fuels based on UN-U_3Si_5 were fabricated, encapsulated in a cladding/capsule configuration and examined with a variety of neutron based techniques to establish their ability to accurately measure chemistry, phase content and isotope distribution, as well as defects and flaws within the rods. The rodlet geometry matches the configuration that will be used for testing these fuels in the Advanced Test Reactor.

Pre-existing inclusions, density, chemical and isotopic inhomogeneities and cracks as well as microstructural features such as phase composition, texture or residual stresses can affect fuel behavior in an irradiation environment. For science based development initiatives it is hoped that certification of new fuel systems can be achieved by fusing science insight with insights from fewer irradiation tests than has been true in the past. However, the goal of accelerated insight from fewer tests places more emphasis on pre-characterizing the condition of test fuel samples prior to irradiation as well as the need for more thorough bulk characterization of the whole irradiated volume to guide destructive examination of irradiated materials. Since neutrons are non-destructive, capable of interrogating whole pellets and sensitive to the mesoscale characteristics being implemented in models, they are uniquely suited for the study of prototype nuclear fuels. Non-destructive 3D maps of cracks, density, isotopic and geometry variation can be measured using neutrons in pellets or rods prior to irradiation. The potential exists for making the same measurements post irradiation. The ultimate goal is to accelerate the time to insight, development and certification of new nuclear fuels.

This initiative is focused on the application of neutrons to draw non-destructive insight on fresh nuclear fuel prior to irradiation and in the future on irradiated fuel. Neutron imaging and scattering techniques easily examine volumes of up to several cubic centimeters, consistent with typical rod assemblies of ceramic fuel pellets. Neutron scattering lengths for high and low atomic number elements are often comparable and allow efficient study of systems consisting of heavy and light elements.

The application of protons [4] and synchrotron X-rays are also under consideration for these studies (though not reported here). Protons, like neutrons, have mean free paths in nuclear materials that facilitate characterization of cubic centimeters of material. The interaction of protons with matter is governed by nuclear and Coulomb interactions. They lose energy in the matter because of Coulomb scattering from the atomic electrons, and scatter from the nuclei both because of the strong interaction and the Coulomb interaction with the proton. Proton radiography is performed by illuminating a target object with a beam of protons and focusing the transmitted protons onto a scintillator screen [5]. Magnetic lenses offer different magnification options. Synchrotron X-rays in excess of 50keV also have applicability to

fresh nuclear fuels and have been used in the study of U-Mo fuel [6]. This established their merit for studies of smaller regions of interest than are typically examined in neutron measurements. In the future a holistic suite of measurement tools might naturally use neutrons, protons and synchrotron x-rays.

Pulsed neutron source's time of flight allows energy sorting for examination of samples by setting the contrast on isotopes or crystal structures. Neutron detector technology has been revolutionized by the use of micro-channel plates (MCPs) for radiographic applications and proved a catalyst for these studies. The micro-channels are coated with neutron absorbing materials such as boron. They currently offer a spatial resolution of 55μm at count rates of 10^8 cm^{-2}s^{-1}. Spatial resolution of 15μm has been demonstrated at lower count rates [7].

At a LANL/INL workshop held in December of 2012 a plan was conceived to use the advanced non-destructive evaluation techniques including neutron and proton radiography available at LANL and INL for analysis of irradiated fuel rodlets from the AFC-2C irradiation at the ATR in Idaho [8]. In the first phase a set of mock-up rodlets were examined containing pellets of depleted uranium dioxide (dUO$_2$) with defects similar to that seen in irradiated fuel rodlets [9]. After these first measurements over the last few years, measurements have demonstrated the applicability of neutrons, protons and synchrotron X-rays to a range of ceramic and metallic fuels [8,10,11], including the ability to measure fission gas pressures [12] and measurements to complement modeling [13]. Several terabytes of imaging and scattering data have been collected. The ability to observe cladding dimensions, cracks, phase and isotopic species nondestructively and in three dimensions has been demonstrated. Development in data analysis and instrumentation is ongoing.

Tomographic analysis of typical fuel/clad geometries using only thermal neutrons can elucidate three dimensional heterogeneities in a few hours. Whereas determination of isotopic species requires measurements of resonances in the epithermal range and measurements on typical clad/pellet geometries typically require a few days of beam time for between 3 and 6 pellets. Diffraction characterization in slices through the sample provides valuable additional information at beam times of about 0.5 days. Although early work focused on UO$_2$, recent initiatives have focused on developing fuels with enhanced accident tolerance, increased burn-up and reduced waste.

2. Neutron Analysis

2.1 Neutrons

Neutrons offer excellent characterization capabilities for nuclear fuels and provide non-destructive insight on mechanical integrity, microstructure, chemistry and crystallographic phase [14]. Measurements are possible at reactors or pulsed sources, but the energy resolution is implicit at pulsed sources and offers capability not efficiently pursued at reactor sources. Recent advances in 2D neutron detection [7] enable improved opportunities for imaging and tomography of nuclear materials. Moreover, time-of-flight (TOF) neutron measurements enable isotope specific tomography. Isotopic densities are deduced from transmission spectra exhibiting neutron resonances, which are recorded for each pixel. Tomographic algorithms allow 3D reconstructions of the spatial distribution of isotopes as well as density and feature heterogeneities. Energy resolved neutron radiography above 1eV is an effective approach for studying samples with compositions that impede measurements with thermal neutrons. By using epithermal neutron energies and assuming known total neutron cross sections of constituents, isotopic enrichment levels can be determined.

Neutrons interact with the nucleus rather than the atomic shell. Thus, their interaction characteristics differ markedly from X-rays. Figure 1 illustrates this by showing penetration depths as a measure of interaction potential for all elements with neutrons, X-rays, and electrons. The data explain why neutron

measurements are more sensitive to light elements in the presence of uranium than X-ray measurements. Since the scattering lengths of neutrons for high and low Z-number elements are comparable in many cases, they are more effective in resolving the elemental contribution of for example uranium and silicon. By contrast, in X-ray diffraction the scattered intensity is biased towards the heavier element. Indeed, for structural analyses of urania determined by diffraction techniques reported and collected in the Inorganic Crystal Structure Database [15], of the 66 experimental structure records for Urania, UO_{2+x}, 55% were measured using neutron diffraction. Neutrons measurements routinely characterize samples as small as a few mm^3 or as large as cm^3.
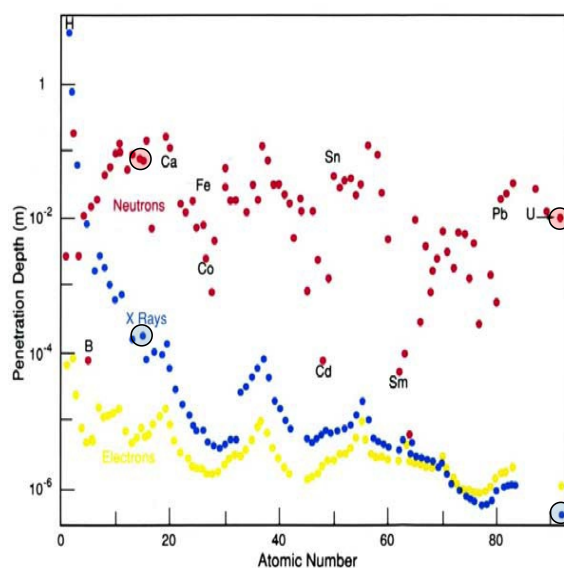
Figure 1: Penetration depth vs element atomic number; neutrons (red), X-rays (blue), and electrons (yellow). Circles highlight Silicon (number 14) and Uranium (number 92).

2.2   Neutron radiography

Imaging with neutrons, protons and X-rays has been applied at LANL to demonstration nuclear fuels since 2010 [4,9]. The primary research focus is on neutrons because of their isotopic sensitivity, their applicability to cm^3 size samples and their potential application to irradiated material. At a pulsed neutron source, the efficient utilization of the time-of-flight technique gives access to neutron absorption resonances which provide a unique finger-print for many isotopes. Energy-resolved neutron imaging, enabled by time-of-flight (TOF) neutrons, can be used at different energy ranges. For example, Lehmann et al. described energy-selective neutron imaging using thermal and cold neutrons [16]. "Energy-dependent neutron imaging with a double crystal monochromator at the ANTARES facility at FRM II" is described by Schulz et al with neutron wavelengths ranging from 2.7 to 6.5A [17]. Strobl et al. describe advances in energy-selective imaging in detail in their review "Advances in neutron radiography and tomography" [18]. New detector technology has expanded the opportunities into the energy regime >1eV as described below. With sufficient penetration and resolution, tomographic methods provide nondestructive measurements of voids, cracks, and density variations. By collecting a series of two-dimensional radiographs, tomographic reconstruction software can routinely produce three-dimensional representations from attenuation-based features.

2.3   Tomographic reconstruction

2.3.1   Data Processing

The detector employed for the energy-resolved neutron radiography stores up to ~3,000 frames corresponding to defined neutron time-of-flight or energy values. Subsequent handling and manipulating the data for tomographic reconstruction is challenging. A significant challenge in developing the routine application of this capability lies in provision of facile user access to the breadth of interpretive opportunity. A few examples are listed below, each of which requires considerable data manipulation.

- Integration over a thermal energy window offers maximum spatial resolution in minimum time (due to spectral characteristics of the Lujan source, Figure 3)
- Integration over a broad epithermal energy range may offer good spatial resolution if resonances from one or more isotopes dominate which are representative of the matrix.
- Integration across one or more discrete energy windows may offer isotopic sensitivity.
- Spectral fitting can be applied to pixel average data or single detector pixels

After raw radiographs are produced for any of the options above, tomographic reconstructions are possible provided multiple projections covering ~180 degrees of sample rotation were collected. The tool used for the 3D- reconstruction in these measurements was TomoJ [19], which is a plugin for the image analysis tool ImageJ [20]. TomoJ is a free software package that was originally designed for electron tomography. In our experience it compared well with commercial reconstruction tools, such as Octopus or VGStudio. To prepare transmission vs. energy spectra for fitting, the raw data was background corrected and divided by also background-corrected open-beam data. Scaling factors to adjust for pixel-dependent variations in e.g. the detector efficiency were determined from an open beam measurement.

Tomographic reconstructions are prone to ring artifacts if pixels are noisy or non-responsive. To filter such artifacts, a ring-filter was applied. This process first required a polar transform of the reconstructed images (normal to the cylinder axis of the pellets and the rotation axis for the tomography). A minimum value for the uncorrected data was set to 60% of the maximum as a threshold for the identification of ring artifacts. Then a one-dimensional median filter was applied with a length of 30 pixels along the stripes. The polar-transformed image was divided by the resultant median-filtered-polar-transformed image to remove the ring artifacts. Finally, the images were transformed back into Cartesian coordinates and the filtered slices were normalized to the original grey-values. The ring filter improves the quality of the CT reconstruction as can be seen by the example shown in Figure 2:
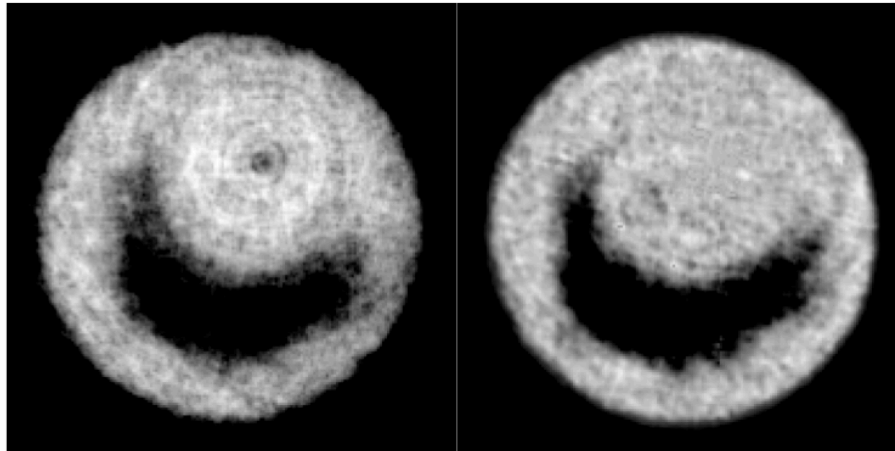
Figure 2: The effect of the "Ring filter" is shown above on a single slice for an accident tolerant fuel pellet; before (left) and after (right).

2.3.2   Thermal and Epithermal neutron spectrum

The neutron beam on flight path 5 at the Lujan Center provides thermal and epithermal neutrons with each pulse, see Figure 3. The moderator is optimized for the thermal spectrum (<0.4 eV). In this neutron energy region, individual projections can take as little as one minute to acquire sufficient counting statistics. Measurements of neutron resonances are typically performed at >1eV for which count-times per projection typically require between 30 and 180 minutes for sufficient statistics to allow for a spectral data analysis.

Thus thermal imaging is an effective and "quick" way to identify the presence of cracks (if the material can be penetrated by thermal neutrons), whereas epithermal imaging of resonances requires longer acquisition times but provides isotope specific insight. Since data for both energy regions are collected simultaneously, the long count times for resonance imaging also provide high quality thermal radiographs. The energy resolution $\Delta E/E$ of a measurement dictates the ability to resolve individual neutron absorption resonances. This results in a tradeoff between the source to sample distance and the energy resolution.
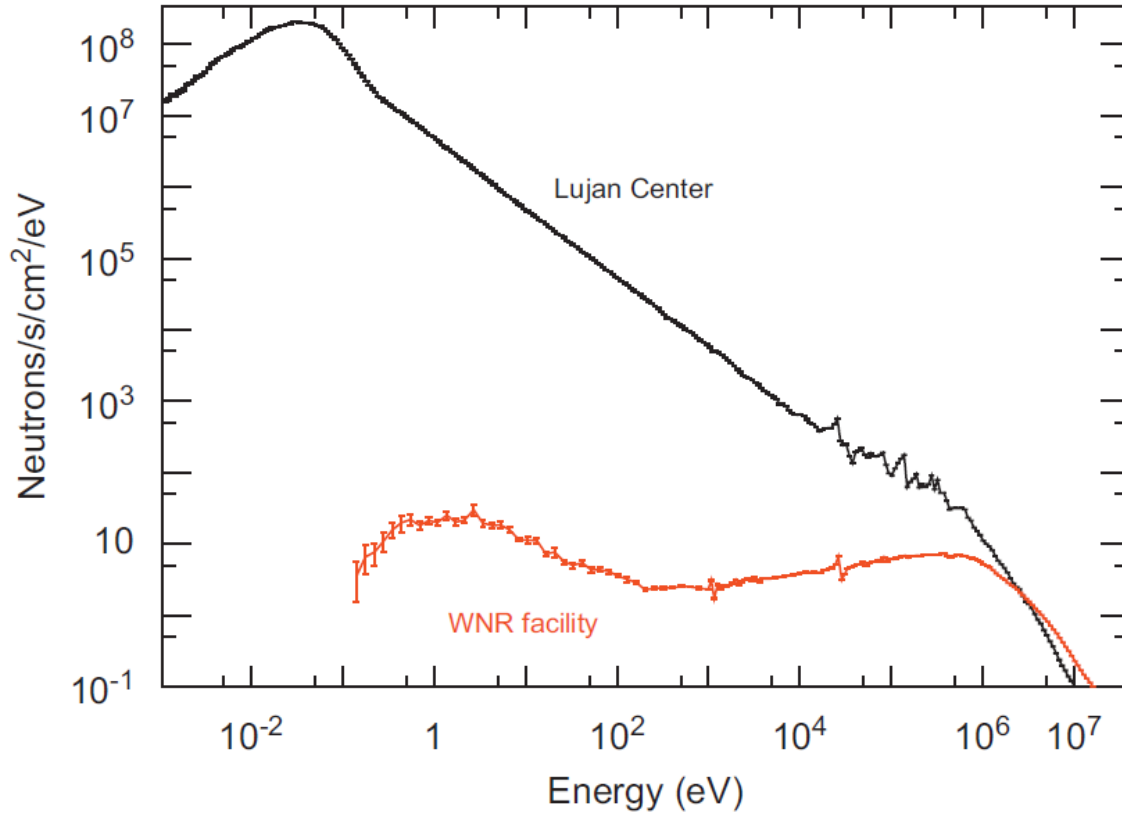
Figure 3: Neutron spectrum produced by the moderator viewed by FP-5, calculated for a proton current of 125 μA (a current if 100 μA was available during the measurements described here) (from [25]).

2.3.3   Resonance Cross sections from ENDF

The energy dependent neutron cross sections associated with isotope specific nuclear absorption resonances provide a material signature necessary for isotope-selective imaging. An enabling capability for these measurements are the tabulated nuclear cross sections in the Evaluated Nuclear Data File (ENDF) database [21]. The database provides cross sections, determined by standardized experimental measurements such as neutron transmission measurements, for individual isotopes. In general, neutron resonances are measurable in a regime of 1ev to 0.1 MeV. Below 1eV cross sections are typically inversely proportional to the velocity of the neutron and do not exhibit "sharp" resonances.

2.3.4   Resonance fitting by SAMMY

Resonance spectra recorded in this study were fit using the SAMMY code (SAMMY, Multilevel R-Matrix Fits to Neutron and Charged-Particle Cross Section Data) [22]. This code was developed by Oak Ridge National Laboratory. It can analyze time-of-flight, cross section data from meV to MeV, where the incident particle is either a neutron or a charged particle. For energies up to several keV, cross sections are generated using the Reich-Moore approximation to R-matrix theory [23]. The code includes a variety of mechanisms to account for normalization, background, and sample thickness as well as options to account for measurement resolution and Doppler broadening. Corrections for self-shielding and multiple-scattering are also available.

Resolved resonance parameters can be output in the ENDF format for inclusion in the evaluated nuclear data files. Bayes' Theorem of generalized least squares is used to find "best fit" values of parameters and

the associated parameter covariance matrix. After data are corrected for background and normalized by the background corrected incident intensity, they are fit with SAMMY. The data input consists of an ENDF database input file with pre-determined resonance parameters (literature values of energies, capture and partial widths and spin numbers as well as the sample element's name, atomic weight and energy range for the data set). Background parameters (constant, linear in energy and time) are varied to account for the efficiency and response of each individual pixel not captured by the original background correction and normalization.

When both the sample thickness and the cross section of the resonance for a given energy are large, the sample can absorb all incident neutrons in a discrete energy range. This causes the transmission to drop to zero and the resonances are described as "black". For attenuation based imaging, a fully absorbed beam will appear as an opaque feature in the transmission image, making tomographic reconstruction impossible since the depth information is lost. However, for resonance imaging, reconstruction with black resonances remains possible by considering energy regions around the resonance. Indeed, in that case they provide an accurate energy specific measurement of the background.

The use of an internal standard can normalize the isotopic measurements and enables determination of accurate partial densities or enrichment levels. For reasons described below tantalum proved best suited for this purpose. It has several narrow resonances in the 1 to 200eV energy range and a foil of known thickness was measured simultaneously with the rodlets. By including a known areal density for the tantalum, the SAMMY resonance fit (described below) can more accurately fit the energy dependent background.

2.4   Calculating enrichment levels from resonance data

To interpret transmission data correctly, it is essential that an accurate background is included. This is crucial if absolute values of areal densities are desired. If the background is not correctly accounted for, then deviations in the measured transmitted intensity introduce errors in the absolute areal density of a given isotope. For this work, a scaled open-beam profile was used as a "baseline" background. The normalized data were then treated with the SAMMY code following procedure described in [24]. The resonance parameters provided by the ENDF database were treated as constants. Background parameters (constant, linear in energy and linear in time) were varied to account for the efficiency and response of individual detector pixels. Then the areal density of different constituents were varied, from which absolute isotopic densities were determined.

2.5   Neutron diffraction

Imaging is complemented by diffraction, which provides insight on crystal structure parameters (space group, lattice parameters, atomic positions, thermal motion etc.) and microstructure parameters such as phase volume fractions, lattice strains (mechanical strain, chemical strain from e.g. interstitial atoms, etc.) and texture (orientation distribution of crystals). While imaging probes length scales on the available spatial resolution (~100 μm), diffraction probes sub-nm length scales with the crystallographic parameters and micrometer length scales with the microstructural parameters. For neutron powder diffraction data analysis, typically full pattern "Rietveld" refinements are performed. From these crystal structure (lattice parameters, atomic positions etc.), microstructure (sample induced peak broadening, phase fractions, texture etc.), and instrument (background, instrument contributions to peak broadening etc.) parameters can be determined.

For the analysis of HIPPO data (see below for a description of the instrument), two software packages are utilized: The General Structure Analysis Software (GSAS) [26] with the automation provided by gsas_language [27] and the MAUD package (Materials Analysis Using Diffraction) [28]. Both packages

provide Rietveld analysis [29] of diffraction data, i.e. minimizing the difference between a function describing the entire diffraction pattern (or multiple patterns simultaneously) and the experimental diffraction data, with the function having parameters describing the instrument (resolution, neutron time-of-flight to d-spacing conversion, incident intensity as a function of d-spacing etc.) and sample (lattice parameters, peak profile parameters, texture). The MAUD package has more sophisticated representations of the orientation distribution function (ODF), including discrete representations, than GSAS, which provides only the spherical harmonics representation [30].

The data were collected on HIPPO using a scan mode. The neutron beam, nominally 10 mm in diameter, is collimated by a 2mm horizontal Cd slit in front of the sample. This illuminates 2mm high disks of the entire volume, i.e. the measured diffraction information originates from a 2mm slice of the sample volume. Using the HIPPO robotic sample changer [32], the sample is moved vertically behind the horizontal slit. To provide information for texture analysis, three rotations around the vertical axis at 0°, 67.5°, and 90° are measured from which the texture information, i.e. the distribution of crystal orientations is derived.
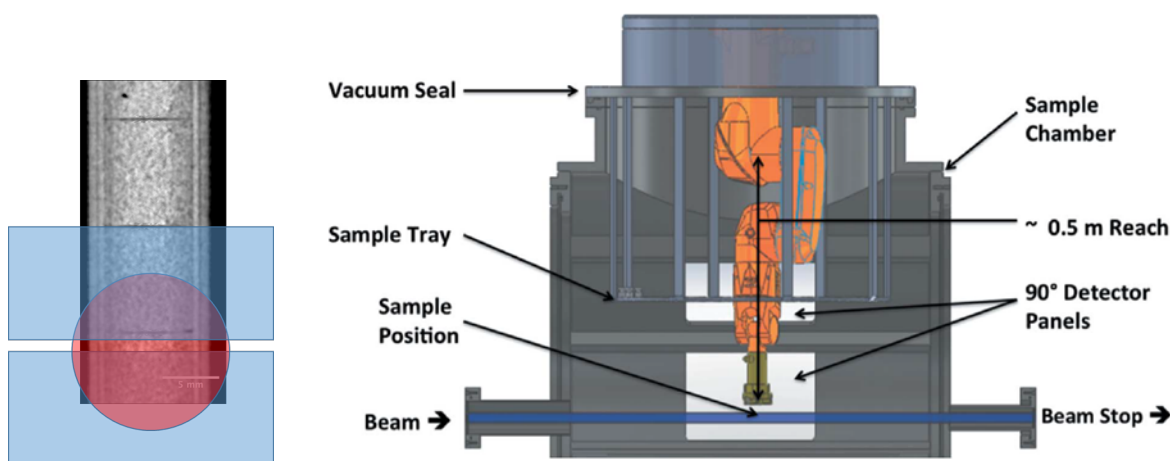
Figure 4: Characterization of nuclear fuels on HIPPO using a scan mode. The beam spot of ~10 mm nominal diameter is collimated with a 2mm Cd slit in front of the sample (left). Using the robotic sample changer (right), the sample is scanned along the axis of the capsule.

Each run on HIPPO collects data with 1,200 ^{3}He detector tubes arranged on 45 panels on five rings with nominal diffraction angles of 144°, 120°, 90°, 60°, and 40°. For weight fraction and lattice parameter analysis, the data from the three rotations around the vertical axis are combined into five histograms, one for each diffraction angle. This randomizes weak to moderate preferred orientations, allowing data analysis assuming a perfectly random powder. The data is then analyzed using a gsas_language script, ensuring the same analysis scheme for all runs.

The texture analysis follows procedures described in detail in [33]. For this analysis, 45 histograms per orientation are analyzed for all three measured orientations simultaneously, i.e. a refinement of 135 histograms. Preferred orientation, or texture, leads to inhomogeneous distributions of the diffracted intensities on a detector ring. Figure 5 below shows intensity variations for different detector panels (displayed as stacks with the diffracted intensity in contours) in the measured data (lower panels). These variations are due to preferred orientation or texture in the crystallographic phase to which the diffraction peak belongs. In the example below, the austenitic stainless steel has a strong peak at ~2.08Å that shows significant variations in peak intensity. The finished analysis (right, top panel) reproduces these variations, indicating a reliable determination of the orientation distribution of the crystals in this phase. Once the orientations distribution is determined, it is represented as pole figures for each phase. It is

noteworthy that this method allows measuring the preferred orientation as a microstructural quantity for all phases detected together with particle size, lattice parameters, and volume fractions.
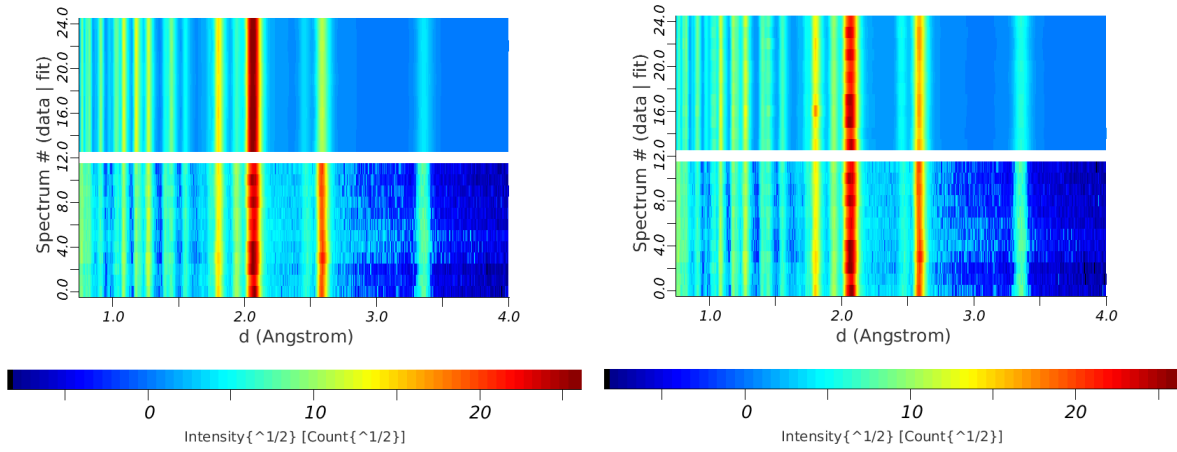
Figure 5: Diffraction data for the twelve HIPPO detector panels on the 40° detector ring for one sample orientation as measured data (bottom panel) and fit (top panel) before the refinement of texture (left), i.e. with random crystal orientations, and after the texture analysis (right).

3.   Instrumentation

3.1   Flight Path 5 (for imaging)

Imaging measurements described in this report were performed using Flight-Path-5 (FP5) at the Lujan Neutron Scattering Center (for a description see M. Mocko et al [25]). It provides a thermal neutron flux of ~ 2.4 10^7n·cm^{-2}s^{-1} at ~8.8m from the moderator with a peak at 25meV. Figure 3 shows the neutron spectrum emitted from the moderator viewed by FP5 to quantify changes in flux as a function of neutron energy. The beam is collimated using borated polyethylene and steel disks with a circular exit collimator. For the measurements reported here the detector was positioned ~ 8.2 m from the source. The fuel rodlets were placed as close as possible to the detector to minimize blur from beam divergence. A collimator (smallest diameter) to sample distance L of about 4.1 m and smallest beam diameter of 2.5 cm (1 inch) resulted in a collimation ratio L/D of 164.   With a sample to detector distance *d* of ~5 cm, the geometric blur is given by *d/(L/D)*≈300 μm (note that this blur is not the same as the spatial resolution). Samples were mounted on a dual rotation stage, allowing to measure two rodlets simultaneously to reduce beam time. The dual rotation stage was mounted on a linear motion stage, allowing translation of the sample in multiple directions for alignment (Figure 7:). As an internal standard, a 0.1 mm thick Ta sheet was placed in front of the sample (source side). To reduce background from gamma radiation emitted from the spallation target, ~12 mm lead was also placed into the beam at the exit of the incident collimator pipe.
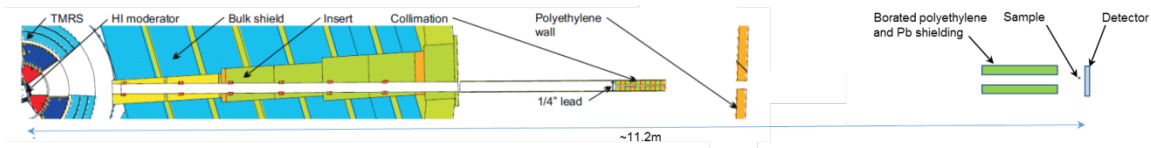
Figure 6: Flight Path 5 Schematic. Note that the polyethylene wall and the borated polyethylene and Pb shielding were not used for the measurements reported here.
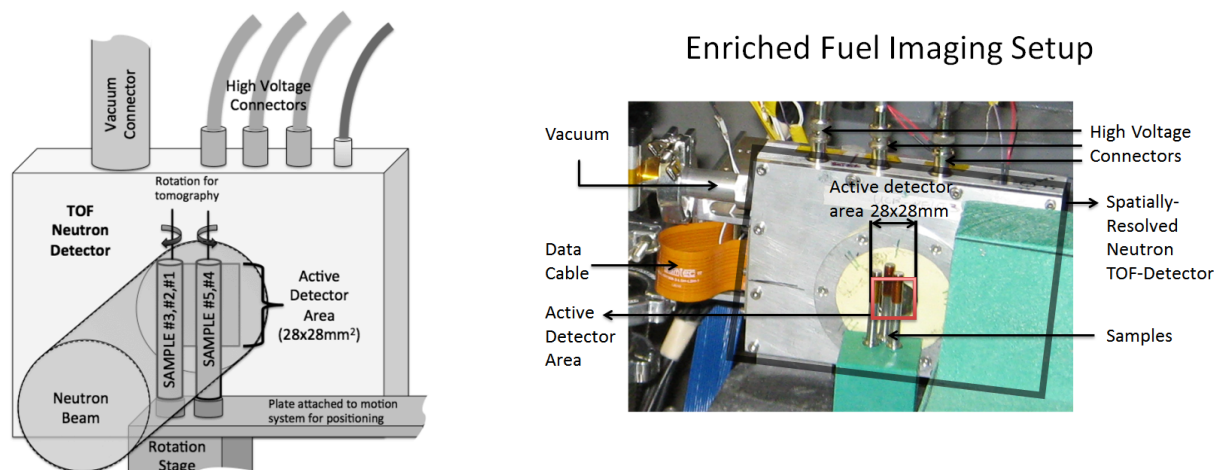
Figure 7: Rodlets in front of detector; Schematic (left), Photograph (Right).

The pixilated neutron time-of-flight imaging detector used at LANL is custom-designed and manufactured by Dr. A. Tremsin (Space Science Laboratory, UC Berkeley). It consists of a Gd/B doped multi-channel plate and MediPix read-out chip [7]. To account for differences in the individual pixel response of the detector, an open-beam measurement was recorded over the entire energy range (0.5 to 200eV). Individual TOF images are divided by the normalized open-beam image. The pixel size of the detector is 55μm with an active area of 512x512 pixels i.e. ~ 28 x28 mm^2.

3.2   HIPPO (for diffraction)

The HIPPO instrument is a general purpose neutron time-of-flight powder diffractometer [31]. Its key characteristics are large detector coverage (1200 ^{3}He detector tubes distributed on 53 panels arranged on five rings around the incident beam) and proximity to the neutron source (~8.9 meters). The short flight path and detector coverage and allow count times as short as one minute and efficient texture characterization. The resolution (Δd/d) in the back scattering geometry is ~ 0.0037 and the 20 Hz repetition rate of the Lujan Center source accesses a d-spacing range from 0.12 to 22°A.   A robotic arm is available for sample changes [32].
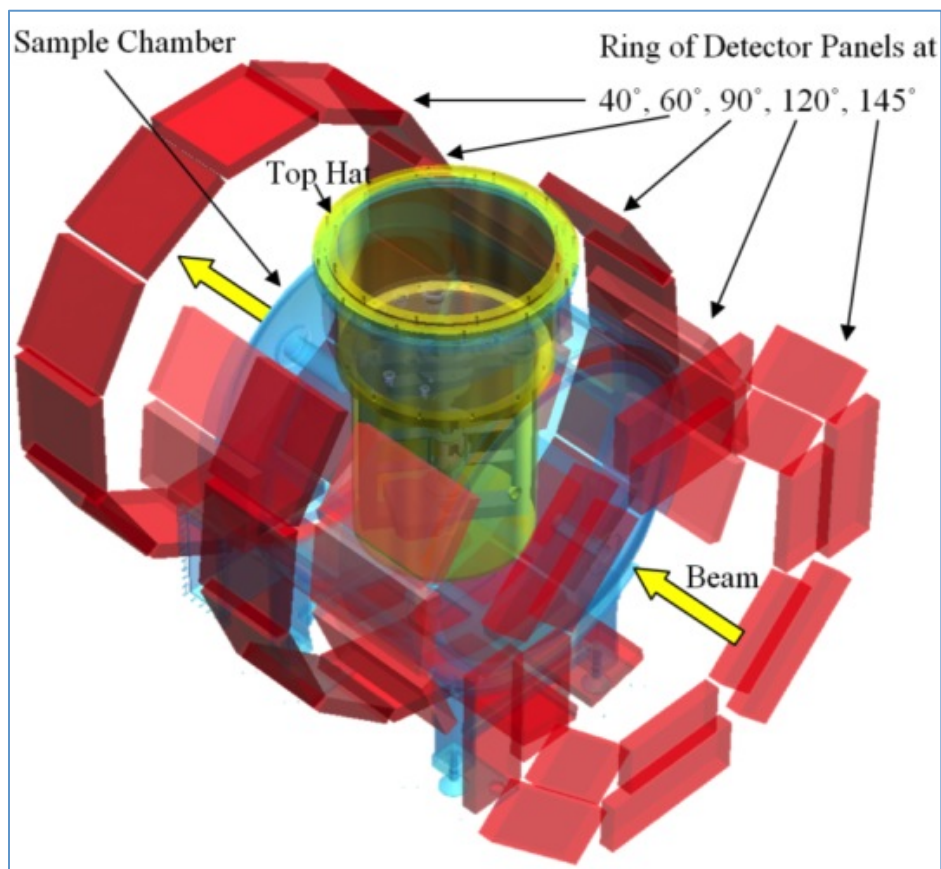
Figure 8: Schematic of general purpose neutron powder diffractometer HIPPO.

4.   Fabrication Details of Advanced Accident Tolerant U-Si Fuel Forms

The Advanced Fuels Campaign within the DOE-NE Fuel Cycle Research and Development Program is developing accident tolerant fuel for commercial light water reactors that will demonstrate improved behavior during design basis and beyond design basis accident scenarios. Uranium-based advanced ceramic composite fuel systems are proposed that will improve the normal and off-normal performance while delivering acceptable neutronic characteristics and maintaining economic competitiveness relative to the commercial UO_2. The pellets characterized in this report are part of this effort. Details of the selection process of fuel forms and background information can be found in a separate report [34].

The synthesis of ATF feedstock materials and fabrication of fuel pellets from the feedstock materials is a multi-step process as shown in the notional flow diagrams given in Figure 9. The U_3Si_5 is made by arc melting stoichiometric amounts of the metallic constituents and the fuel pellets are fabricated by blending/milling the components followed by a conventional cold-press and sinter route. The uranium nitride is synthesized using the carbothermic reduction nitridation process then the UN is blended/milled with U_3Si_5 and pellets are fabricated using a similar process.

U$_3$Si$_5$ Pellet Fabrication   UN-U$_3$Si$_5$ Pellet Fabrication

U Metal	Si Metal

UO2	Graphite

Arc Melt to form U3Si5

Carbothermic reduction

Mill U3Si5 → U3Si5   Mill UN

Blend U3Si5 with Additive

Blend UN, U3Si5, Additive

Press Powder

Press Powder

Sinter Pellets

Sinter Pellets

Centerless Grinding

Centerless Grinding
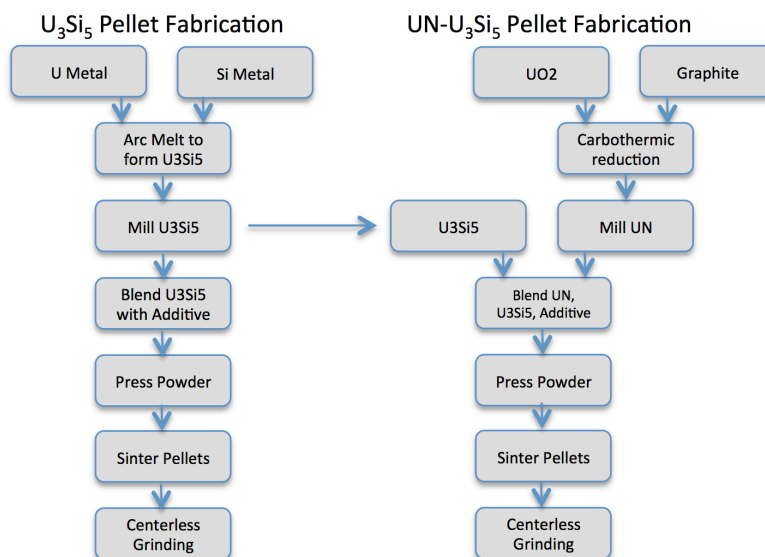
Figure 9: Flow Diagrams for U$_3$Si$_5$ and UN-U$_3$Si$_5$ Fuel Pellet Fabrication.

Following the removal of the U$_3$Si$_5$ and UN/U$_3$Si$_5$ pellets from the furnace, all of the pellets are weighed and measured to determine the final density and record the geometric data in preparation for subsequent processing steps. In addition to the measurements, a qualitative assessment of the quality is made based on cracks, missing surfaces, surface texture, voids, etc. The fuel pellets that pass the quality assessment are then centerless ground to meet the dimensional specification for insertion and encapsulation in the fuel rodlets.

4.1   U$_3$Si$_5$ Feedstock Preparation and Fuel Fabrication

The U$_3$Si$_5$ is prepared by arc-melting stoichiometric amounts of uranium and silicon metals. The arc melting process consists of cutting U metal plate into small pieces that can be placed in a tri-arc furnace for melting. The preparations include removing oxide from the surfaces of the cut pieces to limit the amount of oxides that form on or in the arc-melted buttons. The materials are placed on the water-cooled copper hearth in the tri-arc and the system is sealed and evacuated to purge residual oxygen from the system. In the tri-arc configuration, the titanium getter is continuously heated to ensure the lowest possible pO$_2$ (ideally pO$_2$ < 10^{-15} ppm) within the chamber during the melting of the charge. The material is slowly heated until a uniform melt of the U and Si is achieved. Due to the characteristics of the process, some regions of the melt will solidify first as the arc is removed and these first-cooled regions are more likely to have the composition of a lower melting point U-Si phase. Thus the button must be flipped and re-melted several times to distribute the silicon. After the arc-melting process, the buttons are checked for phase purity using x-ray diffraction.

Fabrication of the U$_3$Si$_5$ pellets followed a conventional cold-press and sinter process. Arc melted U$_3$Si$_5$ buttons ([235]U enrichment of 8.84%) were broken up using a mortar and pestle then milled using a SPEX 8000M mixer/mill and sieved to sub-44 μm. The milled powder was combined with 1 wt.% ethylene bis-stearamide (EBS) and blended for 5 minutes using the SPEX mill. The blended powder was weighed into charges then loaded into the die body and pressed at 100 MPa. The pressed pellets were placed onto sintering trays, loaded into a refractory metal furnace, and sintered. The key fabrication parameters and furnace profile parameters are given in Tables 3 and 4 respectively.

Parameter	Value
U_3Si_5 + EBS blend time	5 minutes
EBS Content	1 wt.%
Pressing pressure	100 MPa
Sintering Temperature	1515ºC
Ramp Rate	5ºC
Sintering time	12 hours
Atmosphere	Gettered Argon

Table 1: Key parameters used to fabricate U_3Si_5 pellets.

Ramp Rate (ºC/min)	Target Temp. (ºC)	Time (minutes)
5	300	55
2.5	340	16
0	340	60
5	1515	235
0	1515	720
10	25	149

Table 2: Set points and ramp rates for sintering of U_3Si_5.

4.2   UN-U_3Si_5 Feedstock Preparation and Fuel Fabrication

Uranium nitride feedstock powder was synthesized using carbothermic reduction nitridation. The urania powder was blended to the target [235]U enrichment then reduced at 950ºC under flowing Ar-H_2 gas to produce stoichiometric $UO_{2.00}$ then the urania is blended with graphite powder. The UO_2+C is thermally treated under vacuum at high temperature and the carbon will reduce the urania and form a uranium-oxycarbide. Nitrogen gas is introduced and the uranium-oxycarbide is converted to uranium-carbonitride. In the final step, N_2-H_2 is introduced to remove the residual carbon and convert the UCN into UN. The UN in milled and sieved to sub-74 µm.

Fabrication of the UN-U_3Si_5 pellets followed a conventional cold-press and sinter process similar to that used to fabricate the U_3Si_5 pellets. The UN was mixed with EBS and milled for 45 minutes. The UN-EBS was combined with 10 wt.% U_3Si_5 powder (equivalent to 15 vol% in UN) and additional EBS. The total EBS content was 1 wt.% of the batch. The blended powder was weighed into charges then loaded into the die body and pressed at 100 MPa. The pressed pellets were placed onto sintering trays, loaded

into a refractory metal furnace, and sintered. The key fabrication parameters and furnace profile parameters are given in Tables 5 and 6 respectively.

Parameter	Value
UN + EBS milling time	45 minutes
UN + U_3Si_5 + EBS blend time	5 minutes
EBS Content	1 wt.%
Pressing pressure	100 MPa
Sintering Temperature	1775ºC
Ramp Rate	5ºC
Sintering time	12 hours
Atmosphere	Gettered Argon

Table 3: Key parameters used to fabricate UN-U_3Si_5 pellets.

Ramp Rate (ºC/min)	Target Temp. (ºC)	Time (minutes)
3	300	92
0	300	30
10	1775	150
0	1775	720
10	25	175

Table 4: Set points and ramp rates for sintering of UN-U_3Si_5.

4.3 Fuel Fabrication Results

After centerless grinding, all pellet diameters were measured and evaluated for condition defects. The average pellet density and diameter for each of the three compositions is shown in Table 7. The target density of 95% theoretical was achieved with the U_3Si_5 batch of pellets and UN(4.95)-U_3Si_5(8.84) and UN(2.7)-U_3Si_5(2.7) pellets were just below at 93% and 94% respectively. The average pellet diameter for all three batches met the target specification value of 0.325 inches. The overall pellet quality was very good, however several of the pellets that did not pass the quality inspection showed signs of end capping. Optical images of a sub-batch of U_3Si_5 pellets is shown in Figure 10 along with an image of a centerless ground UN-U_3Si_5 pellet. Figure 11 shows an X-ray diffraction pattern from a powder sample of a UN-U_3Si_5 pellet. The figure shows a series of peaks associated with the primary UN phase and also the characteristic peaks for the secondary U_3Si_5 phase. The X-ray results are indeterminate with respect to the presence of other U-Si or oxide phases.

Composition (^{235}U enrichment)	Average Density (% theoretical)	Average Diameter (inches)
U_3Si_5 (8.84)	95.1	0.325
UN (4.95) - U_3Si_5 (8.84)	93.0	0.325
UN (2.7) - U_3Si_5 (2.7)	93.8	0.325

Table 5: Summary of average pellet density and diameter for all three compositions.
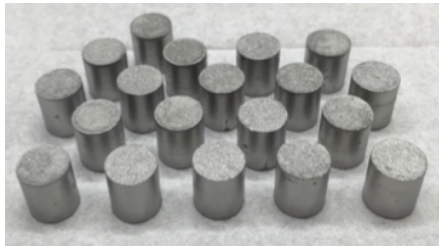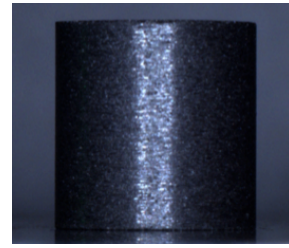
(a) as-sintered U_3Si_5 pellets   (b) centerless ground UN-U_3Si_5 pellet

Figure 10: Optical images of (a) as-sintered U_3Si_5 pellets and (b) centerless ground UN-U_3Si_5 pellet
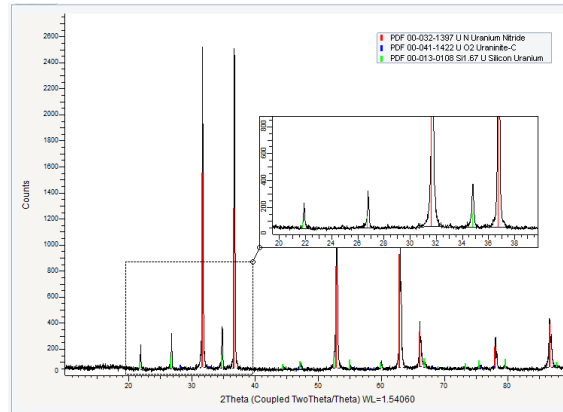
Figure 11: X-ray diffraction pattern of powder sample from UN-U_3Si_5 pellet.

A sample UN-U_3Si_5 pellet was cross-sectioned, ground, and polished for optical microscopy (Figure 12). The grey phase is UN, the light colored phase is U_3Si_5, and the black regions are pores. Several important features are revealed in this image. The green pellet prior to sintering is made of compacted UN, U_3Si_5, and EBS powder. During the early stages of sintering, the EBS will volatilize and boil off leaving a void fraction in the compact of ~30%. As the furnace reaches the sintering temperature of 1775ºC, the U_3Si_5 melts and forms a liquid phase that begins to fill the void volume under the action of capillary stress gradients. The U_3Si_5 liquid facilitates UN particle rearrangement, and also enhances mass transport at the surface of UN particles, decreasing the radius of curvature of irregularly shaped particles, and forming a more spherical geometry thus lowering the surface free energy. As the furnace temperature decreases to the U_3Si_5 solidus temperature, the solid U_3Si_5 phase will begin to precipitate, filling the inter-particle space and leaving very little porosity in the solid U_3Si_5. The majority of the retained porosity in the fuel pellet is located in the UN phase. In the upper central area of the image, micro-cracking is evident in the

solid U_3Si_5 phase and this may be the result of a volume change associated with a phase transition at ~450ºC identified from heat capacity measurements by White [35].
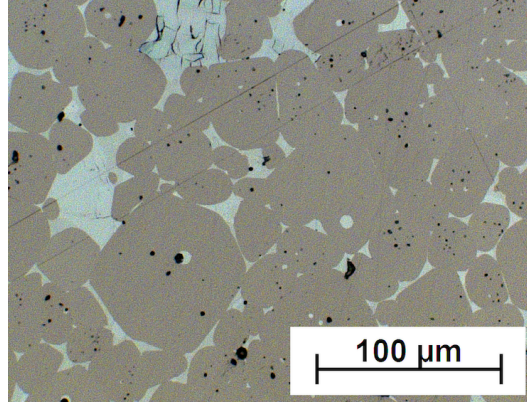
Figure 12: Optical micrograph of UN-U_3Si_5 pellet cross-section.

4.4   Sample Container

The pellets were loaded into cladding or rodlet (inner container) and capsule (outer container). The rodlet is made of Kanthal AF, a ferritic iron-chromium-aluminum alloy (FeCrAl alloy) characterized by excellent oxidation resistance and very good form stability and typically used as heating elements. The capsule is 316L stainless steel. The dimensions of the container and the schematic of the entire assembly are shown in Figure 13. The 64 μm (cladding - capsule) and 76 μm (pellet cladding) radial gaps of the assembly are a useful benchmark of the imaging and CT resolution of the setup reported here.
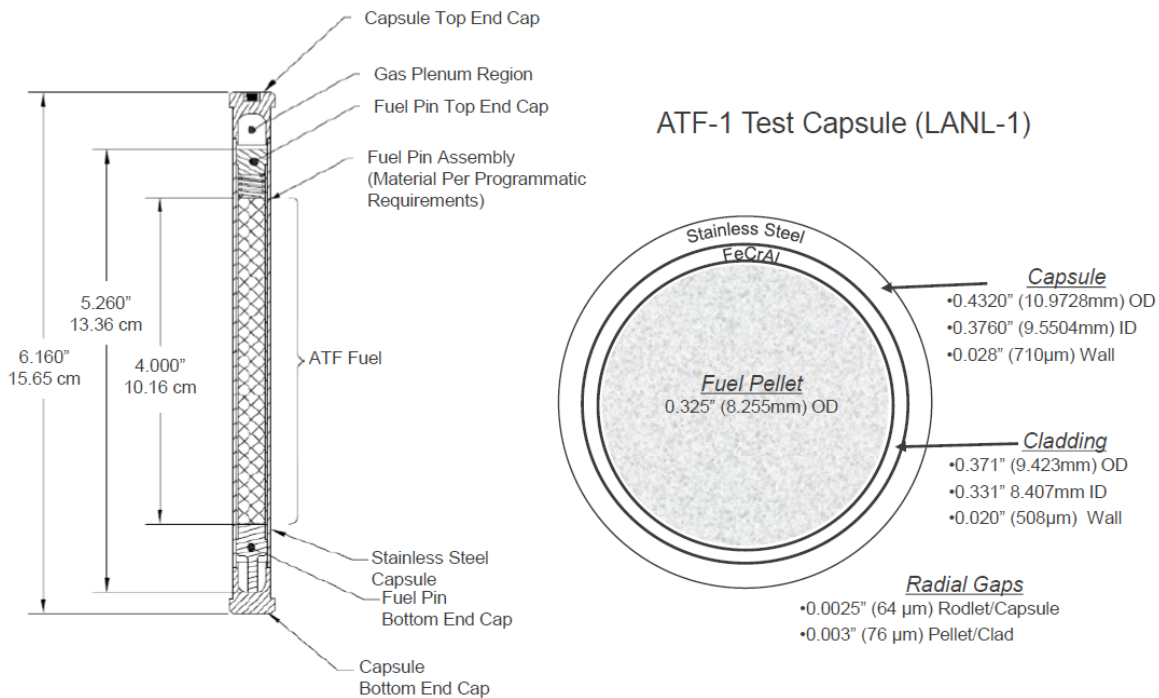
Figure 13: Schematic of the ATF-1 Test Capsule (LANL-1) rodlet and assembly configuration.

5.   Results

5.1   Energy-Resolved Tomography

The pulsed neutron source at LANSCE in combination with a pixilated neutron time-of-flight imaging detector allows quantitative analysis of areal densities for individual pixels or regions of pixels. Due to difficulties with the detector and beam delivery, only partial results are presented. In general, the number of rotations for tomographic reconstructions is a compromise between available beam time and resolution of the CT reconstruction. Instead of rotations from 0º to 180º with a constant increment, for current measurements at FP-05 the golden ratio is used to break the 180º total rotation range into non-constant increments with approximately 90º angular offset [36,37]. The benefit of this data collection strategy is the ability to reconstruct meaningful CT data from any number of recorded projections with increasing resolution, whereas constant increments require a full dataset, covering the full 180º rotation range for a meaningful reconstruction. Additionally, isotope specific information is extracted from absorption resonances in the cross section for individual isotopes

5.1.1   Cold vs. Thermal vs. Epithermal Neutron Tomography

Figure 14 shows a thermal neutron attenuation image of LANL-ATF-MU-LadC top and LANL-ATF-MU-LAdUS bottom. Due to the low ^{235}U enrichment of the fuels, cold neutron energies offer best contrast for cm-sized fuels containing ^{238}U only. With a total neutron cross-section for ^{238}U of ~23 barn at 1 meV, ~12 barn at 25meV and ~10 barn at 1eV, epithermal neutrons do not provide better contrast compared to thermal neutrons as compared to ^{235}U.While selecting epi-thermal neutrons with our setup is routine, epi-thermal neutrons are also available at a reactor source. This may allow utilizing this insight by fully shielding the thermal neutron beam at a reactor source, e.g. with a Cd sheet and collect open beam and sample radiographs in that configuration. Radiographs collected with epi-thermal neutrons only allow more reliable characterization of materials fully attenuating the thermal neutron beam, such as for fuels with high ^{235}U enrichment. For the case of low ^{235}U enrichment, the epithermal and thermal response for ^{238}U are similar for regions that do not contain absorption resonances. Therefore, separation of the spectra using a Cd filter would not add additional insight.

Due to difficulties in beam delivery and detector failure for FY16/17 run-cycle, the fuels are currently being remeasured to gain isotope specific information of the fuels based on the energy-specific fingerprints of the individual isotopes. Furthermore, pixel-centroiding, as described in detail in the following chapters, is also implemented in the current acquisition mode, which will allow characterizing these samples to a higher spatial-resolution (see following chapters). This report contains a preliminary assessment of fuel rod LANL-ATF-MU-LadUS based on thermal tomography.

(a)

(b)
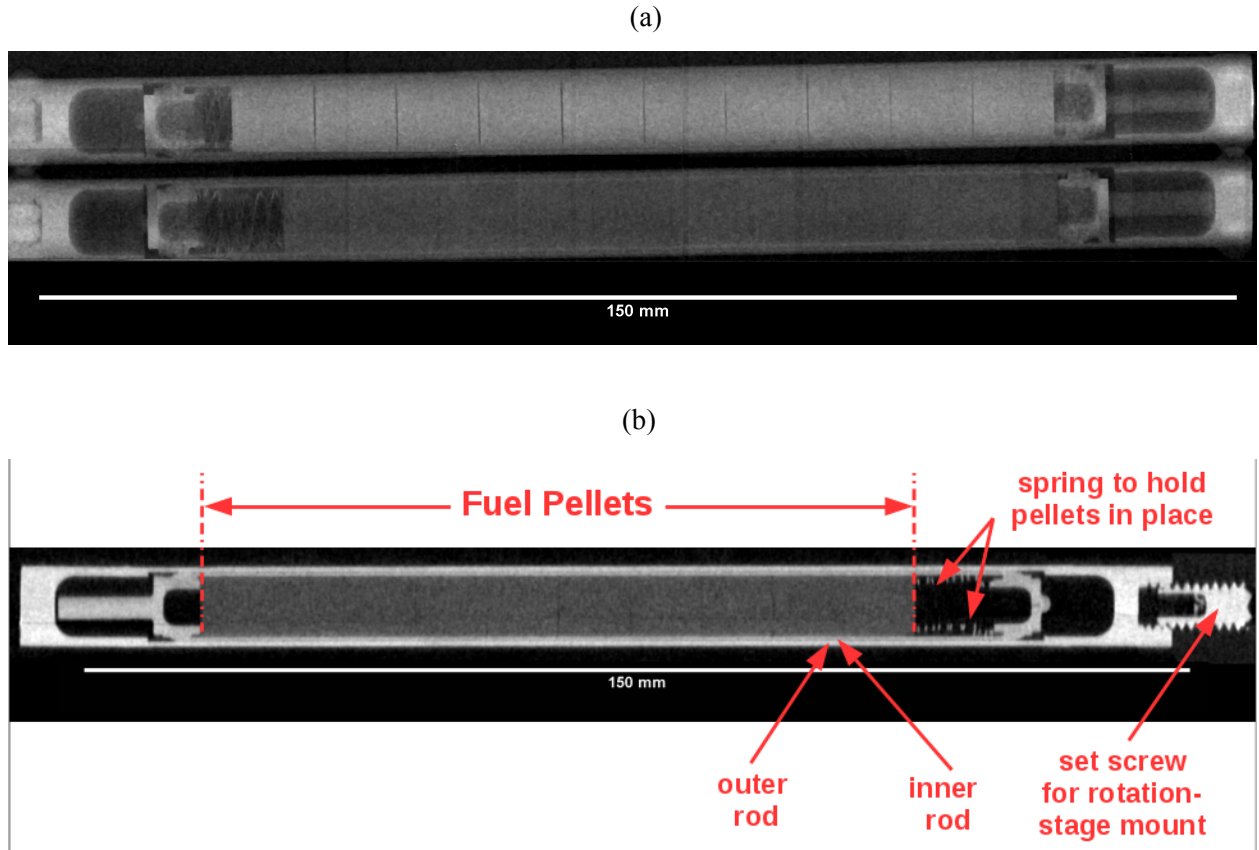
Figure 14: (a) Thermal neutron attenuation image (integral of ~1 meV to ~60 meV) of the two assemblies LANL-ATF-MU-LadC top and LANL-ATF-MU-LAdUS bottom. Spacers, inner and outer cladding are visible. (b) Thermal neutron reconstruction. Slice along the cylinder axis of LANL-ATF-MU-LAdUS .

5.1.2   CT Reconstruction of LANL-ATF-MU-LAdUS

Due to the relatively low cross section of ^{238}U, the entire integrated energy spectrum is used for tomographic reconstruction to maximize the statistics for each projection. A total of 108 projections with 30 sec acquisition time per projection were recorded. The active detector area of 28 by 28 mm^2 requires scanning of the sample to capture the total length of ~ 16 cm of the fuel rods. Consequently, six individual tomographs at different locations in height along the cylinder axis were acquired using a high precision translation stage for position accuracy within a single pixel (55 µm). Finally, the six translations were stitched together, resulting in a single large data-set with an image size of 512 by 3072 pixels. The total stack containing all projections was then used for the tomographic reconstruction of the fuel rod. The resultant reconstruction of LANL-ATF-MU-LadUS does not show significant variations in the attenuation of the fuel pellets greater than 6%, as well as no features observed within the pellets that are larger than 150 µm in size with sufficient contrast. As mentioned before, due difficulties in FY16/17, measurements are being repeated for accurate determination of isotope concentrations and feature detection.

5.2   Diffraction

Neutron diffraction data of the LANL-ATF-MU-LAdUS capsule were collected on the HIPPO neutron time-of-flight diffractometer at the LANSCE facility.   The diffraction data complements neutron tomography data collected on the same specimen. However, due to experimental problems towards the end of the 2016/17 run cycle (July 2016 to January 2017 with the samples delivered to LANSCE in November 2016) and accelerator problems in the 2017 run cycle (July 2017 to December 2017 with production beam delivered only after mid August and this report due in mid September), only this sample could be characterized by neutron diffraction.

Diffraction data analysis was performed against data from four histograms simultaneously, i.e. common parameters such as lattice parameters, atomic displacement parameters and weight fractions match all four data sets. Background or peak width parameters are independent for each phase and histogram. A total of 58 variables was refined against the data from the four histograms collected with the 140°, 120°, 90°, and 60° diffraction angles. Figure 15 shows an example of four refined datasets. The data from the 40° bank was excluded due to the poor resolution (note the increasing diffraction peak width with decreasing diffraction angle Figure 15). For the refinement of lattice parameters, indicative of strains due to mechanical deformations or chemistry changes, the austenite phase lattice parameter was used as an internal standard for each slice, i.e. changes in the lattice parameters or unit cell volumes of the other phases are relative to the austenite phase. Assuming that the outer capsule remained unchanged, this allows measuring lattice parameter changes in the other phases independent from possible changes of the center of gravity
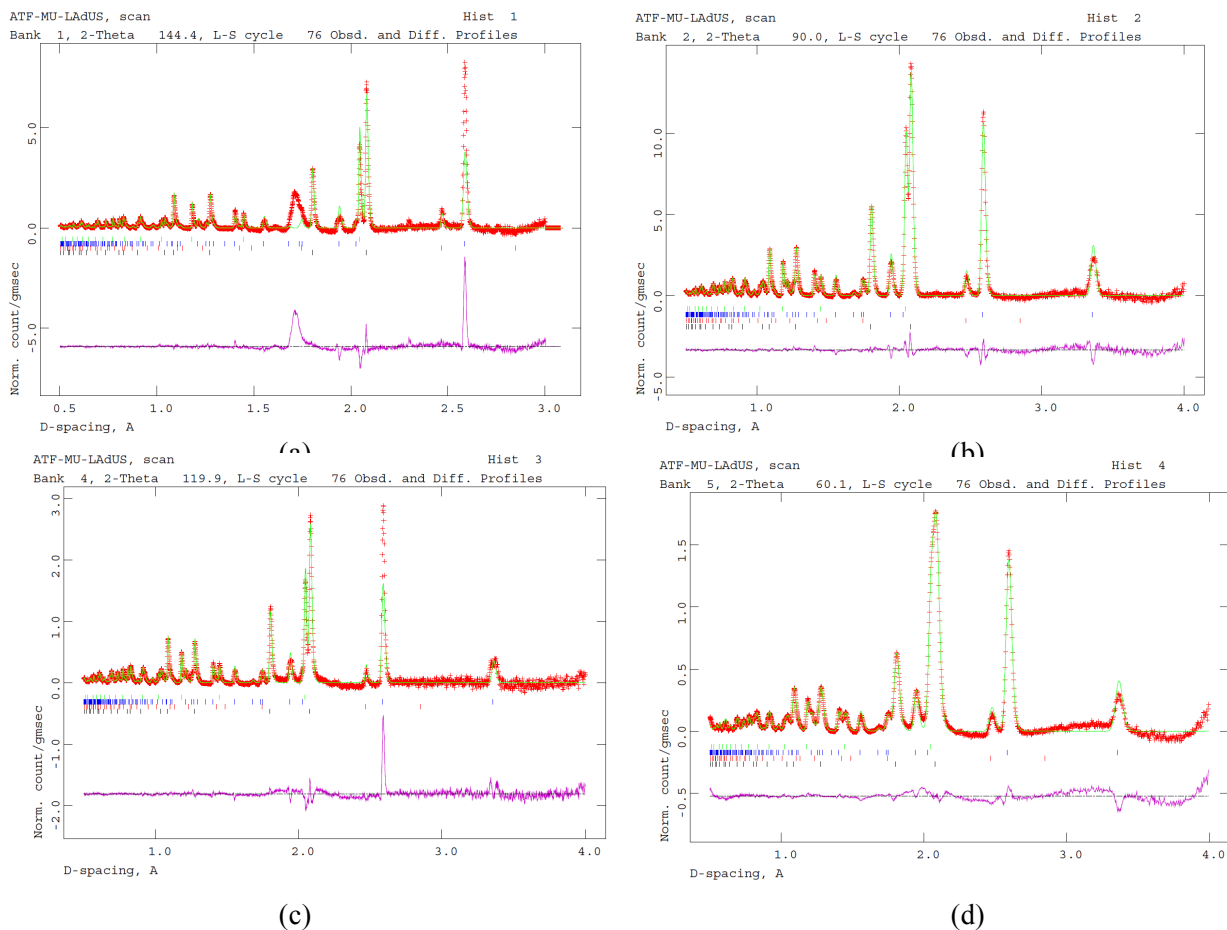
Figure 15: Diffraction data collected on HIPPO (red crosses) and Rietveld fit (green curve) with difference curve between data and fit for the scan at 148 mm, i.e. in the center portion of the capsule (fuel ranges from 180 to 80 mm). The Tick marks below the experimental data and fit indicate calculated peak positions for austenite (black, bottom row), UN (red, 2nd row from bottom), U_3Si_5 (blue, 3rd row from bottom) and ferrite (green, top row). Note that the ~1.7A results from neutron background at 8.3 ms from protons passing at 100 Hz to the LANSCE target-4/WNR, only the backscattering back is in a geometry to capture that background.
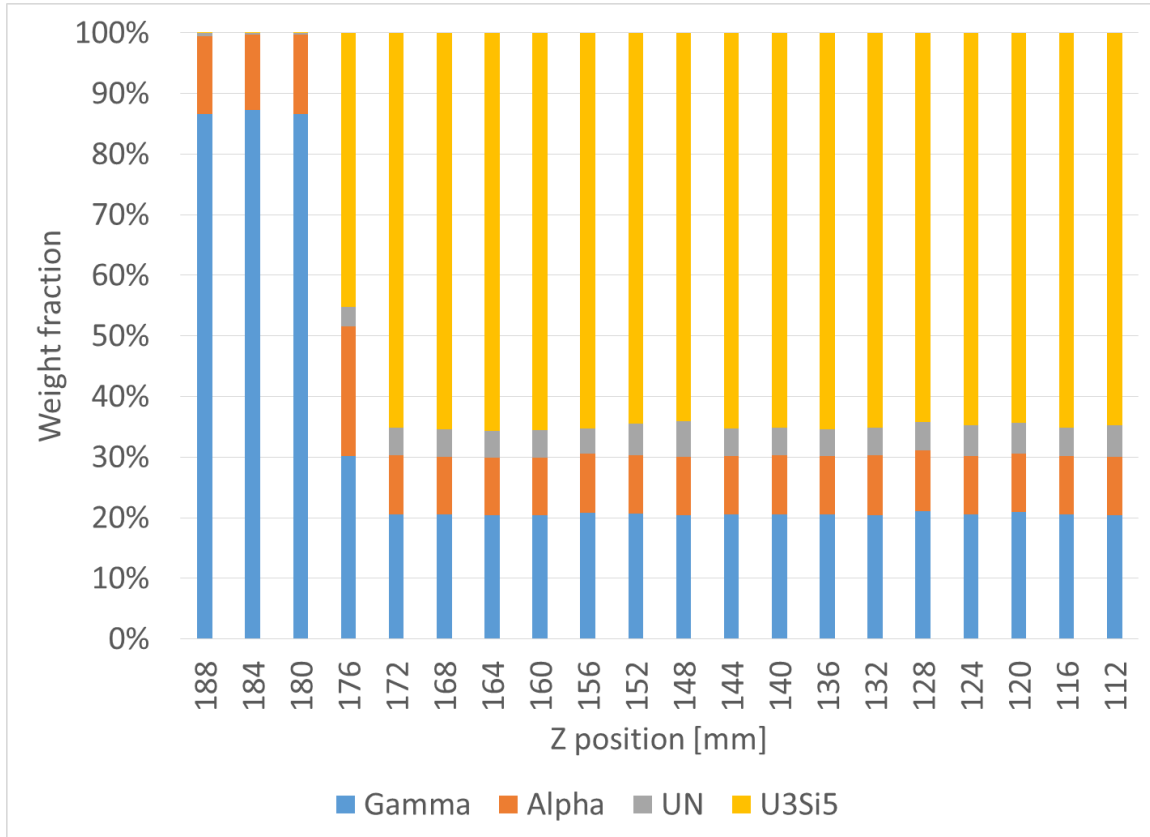
Figure 16: Weight fractions as a function of vertical position derived from the GSAS analysis of the sum of the three sample rotations collected for each sample position.

The weight fraction data shows no significant deviations in composition for the scanned positions. The fuelt pellets were nominally pure U_3Si_5 pellets. The 3 to 5 wt% UN is therefore considered a contamination in U_3Si_5 produced during an earlier stage of the development of the U_3Si_5 capability at LANL, when the uptake and release of N_2 from the W fixturing was not yet appreciated. Neutron diffraction is therefore an efficient tool to also verify fuels during development of synthesis routes. For the pellet homogeneity, this finding indicates that all pellets in the stack are homogeneous in phase composition.
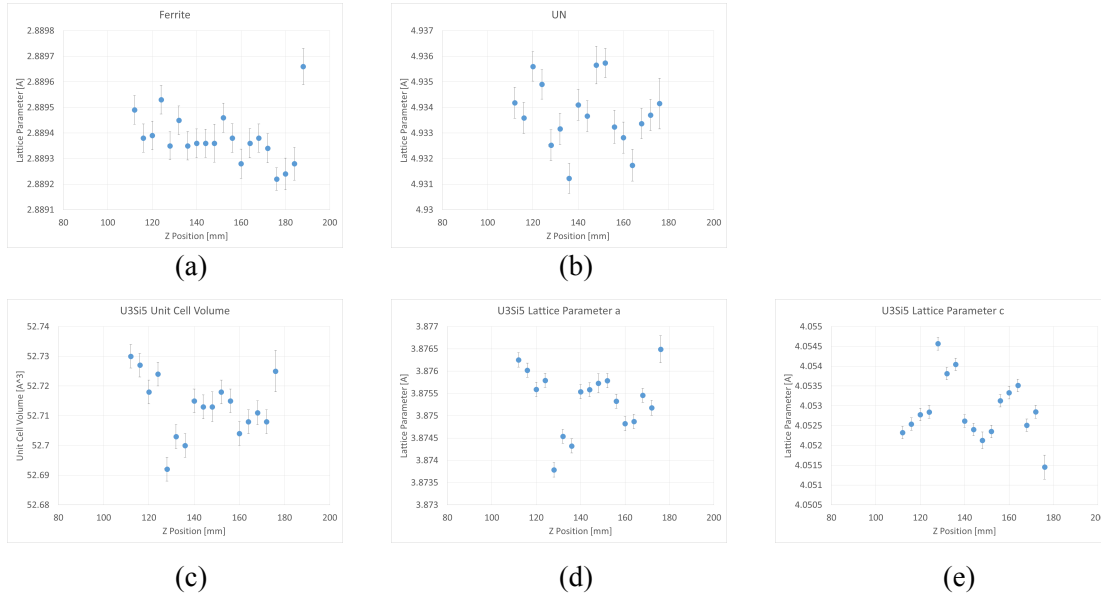
Figure 17: Refined parameters of the Rietveld analysis of the diffraction data collected for the scan.

While the ferrite and UN phases show no systematic variation of the lattice parameter as a function of positions, the U_3Si_5 lattice parameters appear to cluster in sets of four data points. With a scan increment of 4mm and a pellet height of 8mm, this would indicate that pairs of pellets have similar lattice parameters. Since U_3Si_5 melts during the processing, this could be potentially explained with changes in chemistry, i.e. absorption of nitrogen atoms into the silicide lattice. Scans with a smaller increment would add data to understand this observation.

Besides the data analysis of the datasets consisting of the sum of all data from each sample rotation, the same data was also processed for texture analysis using the MAUD software. Figure 18 shows pole figures for the four phases measured in the LANL-ATF-MU-LAdUS capsule: Austenite from the 316 stainless steel capsule, ferrite from the Kanthal rodlet, UN and U_3Si_5 from the fuel pellets. Both steel phases exhibit a fiber texture with cylindrical symmetry typical for drawing processes. The UN phase shows a weak fiber texture, possibly from the pressing. The U_3Si_5 shows some asymmetric preferred orientation, best visible in the c-axis pole figures (001). Occasionally, stronger maxima occur e.g. in the 002 pole figure (crystallographic c axis). This could be indicative of larger interconnected volumes re-solidifying as a larger single crystal. The data analysis is done on the same data as shown above for the Rietveld analysis with GSAS with a different data reduction of the raw data (creation of 45 histograms for each of the three rotation, resulting in 135 diffraction patterns instead of five) and using a different analysis tool (MAUD instead of GSAS). Together with the observation of changes in the crystal lattice parameters described above, this would indicate that the U_3Si_5 phase is the main source of inhomogeneities in this sample. The changes are small and e.g. modelling of the mechanical stresses induced during cooling from >1700°C of an anisotropic hexagonal crystal could provide insight whether these observations could explain for instance cracking of these pellets during re-heating.
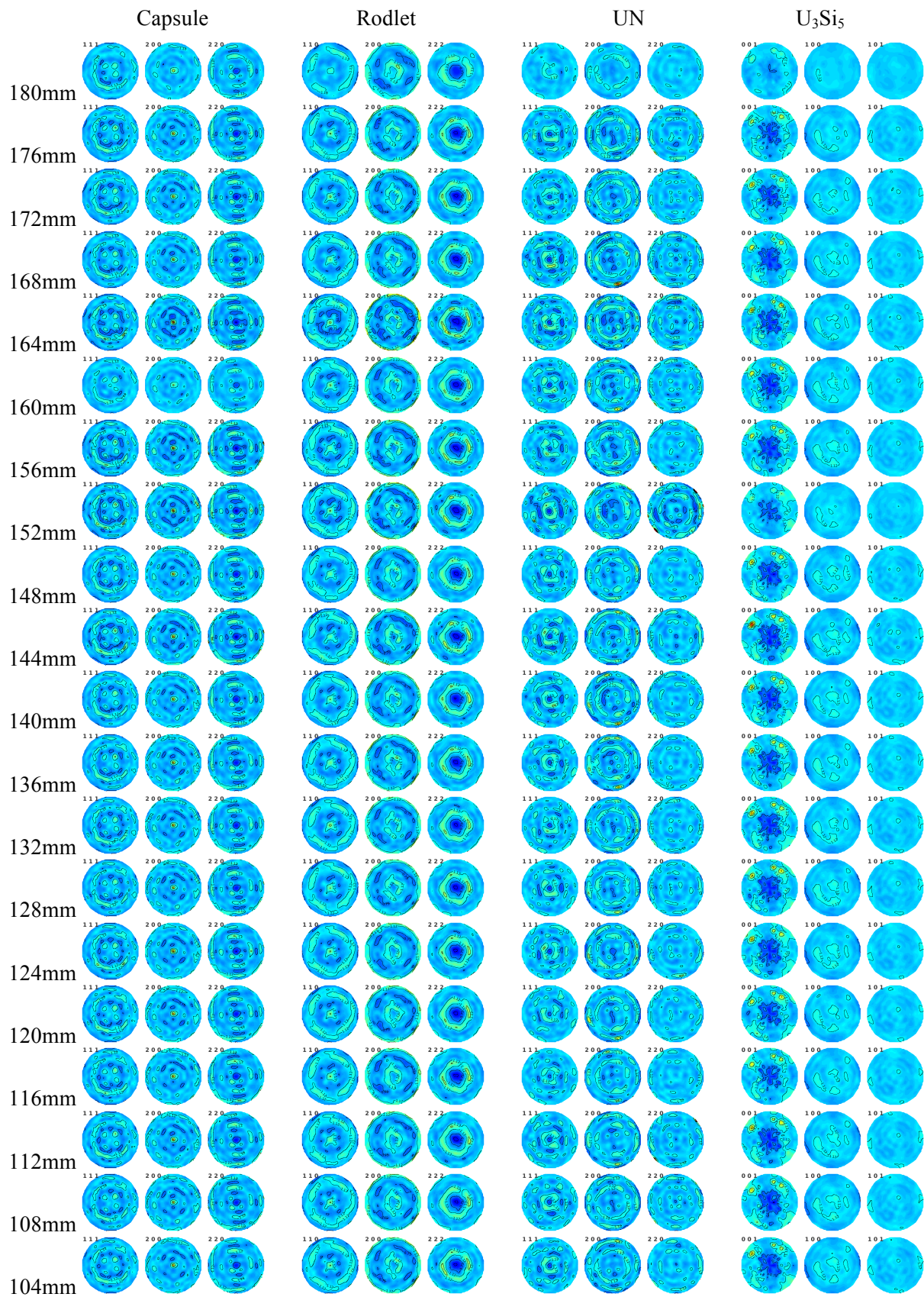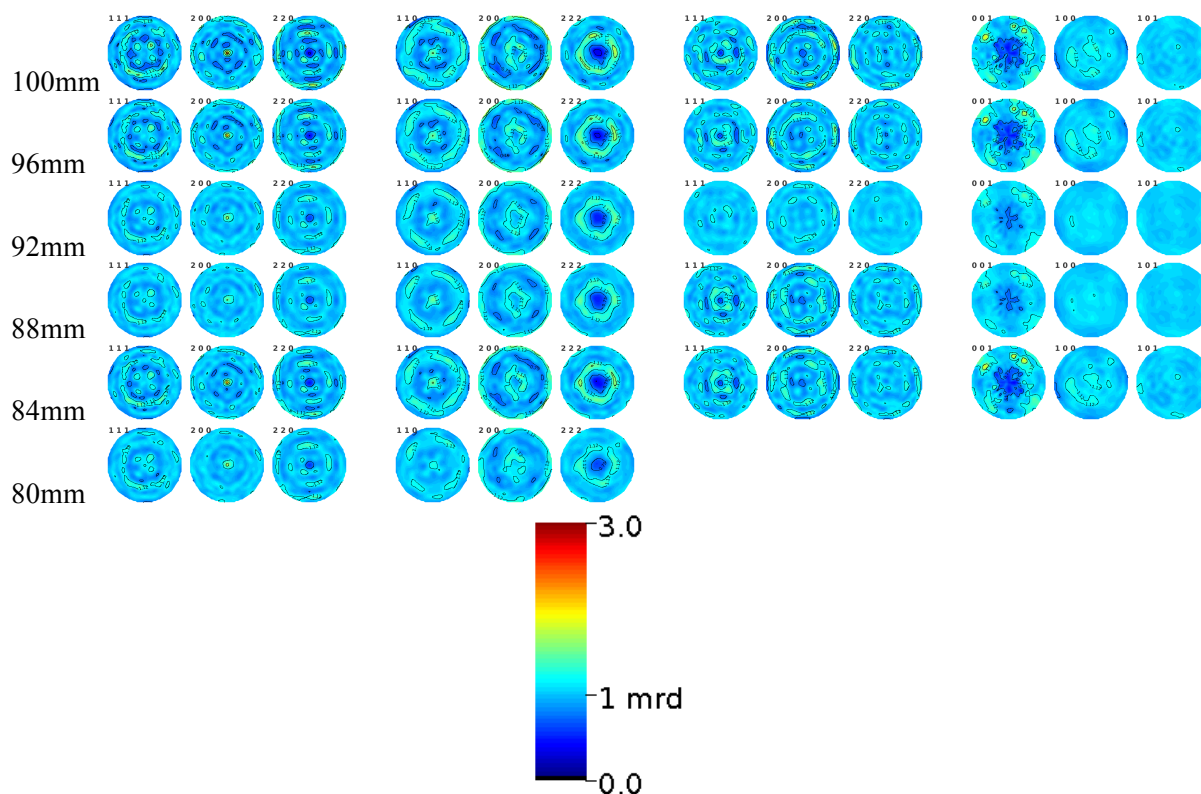
Figure 18: Pole figures for the four phases detected in the capsule LANL-ATF-MU-LadUS. For all pole figures, the capsule axis is in the center of the pole figure.

From the Maud analysis, weight fractions are also determined. These are in principle more accurate than the determination using GSAS and single histograms assuming a random powder since the diffracted intensity is more accurately determined when texture is included.
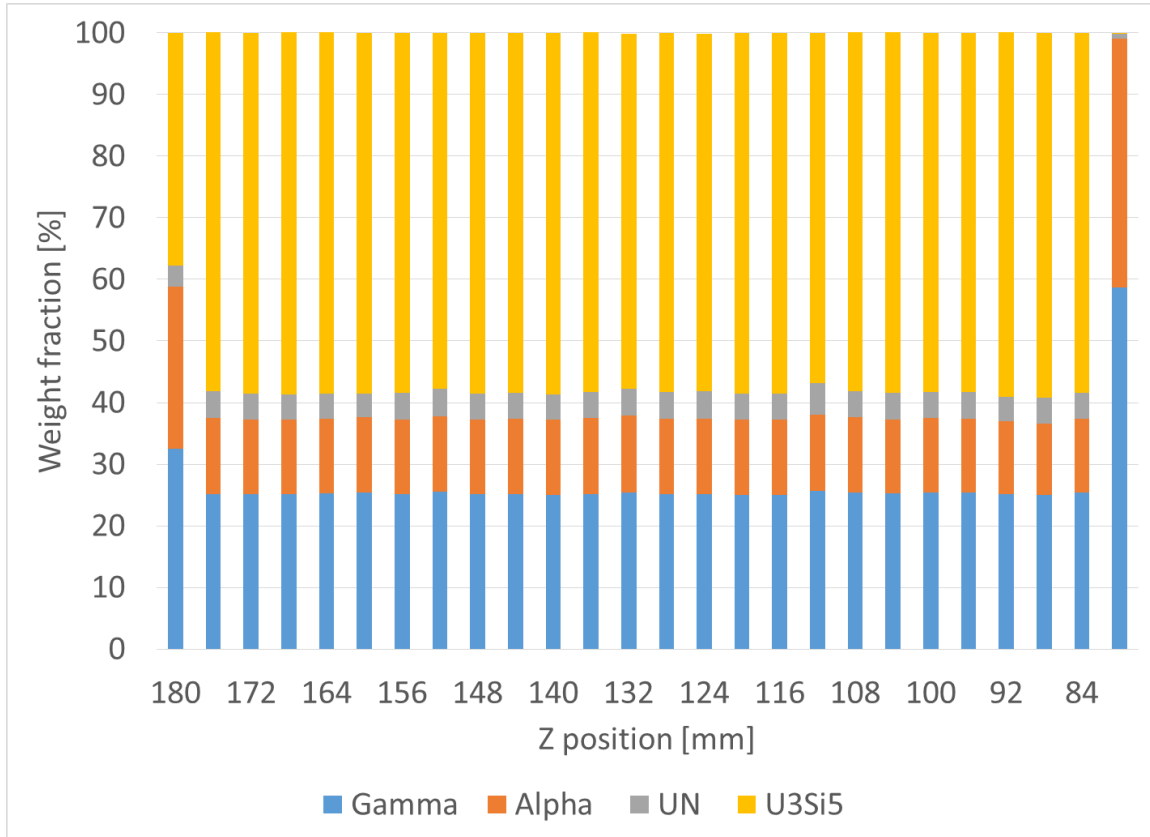
Figure 19: Weight fractions as a function of position

6.   Method Development

The energy-resolved neutron imaging technique is undergoing rapid development. During the period of the work reported here, two new capabilities were achieved that will lead to improved characterization capabilities for the NE mission in the future. First, pixel centroiding was implemented on the imaging detector used here that will lead to an improved resolution by a factor of two to three. Second, a 500 MHz event rate detector with 55 photomultiplier tubes viewing 55 [10]B loaded liquid scintillator volumes was revived after a decade long hiatus [47]. Both advances are discussed in some detail below.

6.1   Pixel Centroiding

The results of high resolution neutron radiography experiments presented in this report, demonstrate the sub-pixel resolution capability while preserving the energy resolution data. Single neutron-counting data taken, the center of mass algorithm for the centroiding, and parameter settings for increasing the resolution are presented. Thresholds are discussed for event recognition in the case for overlapping events and possible gamma rejection. Quantitative assessment of the resolution indicates an initial increase of the resolution from ~80μm to ~20 μm

6.1.1   Introduction

Pulsed neutrons are an ideal modality for imaging nuclear fuel due to penetration through lead and cladding material. Different from X-rays and electrons, neutrons interact with the nuclei of atoms and allow studying distribution and quantification of hydrogen and non-destructive isotope density

measurements as described above. Current methods of neutron pixel centroiding involve charge pulse mode with the detector and sacrifice energy resolved measurements [48]. This advancement is relevant to general capability development with application to the Fuel Cycle R&D Program by increasing resolution to 11μm, allowing for instance the typical pellet-cladding distance (71 μm +/- 5μm) to be accurately characterized while preserving the capability of energy resolved neutron imaging (ERNI) at high resolution.

6.1.2   Setup

The Medipix/Timepix MCP detector at the Los Alamos Neutron Science Center (LANSCE) facility allows single neutron event detection due to the high detection efficiency (50%-70%) [49] and has a 100kHz frame rate in single particle mode. The Timepix detector is a microchannel plate (MCP) doped with boron and gadolinium and coupled with another stack of MCPs to provide amplification. The hole size for the doped MCPs are 8 μm and the amplifiers have 10 μm holes. The detector sensor utilizes a CMOS chip with four 256x256 arrays of pixels with a 55 $μm^2$ pixel size [50]. The detector is held under vacuum and can give energy resolution by the time-of-flight method with the supply of a time zero event pulse. The detector is installed in flight path 5 at typically ~10 meters from the source at LANSCE. For the measurements presented here, the beam was collimated down to 0.5 cm to provide a collimation ratio L/D of 200.

6.1.3   Center of Mass Centroiding

Centroiding has been used in digital microscopy since 1978 [51] to achieve sub-pixel high resolution and converting this technique to neutron imaging is relatively new. Multiple pixels are activated when a neutron impinges on the detector. The location of the neutron can be calculated by computing the center of mass or centroid of the activation distribution. Each 55μm pixel is divided into 25 sub-pixels and this will result in an increase the effective resolution to 11μm. One complexity with centroiding is if there is a double or triple interaction with multiple neutrons overlapping on one frame, the center of mass cannot be distinguished and the calculation will fail, but in pulse charge mode it is possible to distinguish up to 50% overlap. However, this can simply be adjusted by taking a shorter acquisition time and negating any event that is bigger than 20 pixels or smaller than 2 pixels (user determined). This allows the possibility to discriminate between electronic noise and a multiple particle overlap. Utilizing a larger stack size, we can theoretically achieve a magnitude increase in spatial resolution to 5μm, however, realistically the gain is limited by the MCP pore size to about 11 μm.

A single particle event in integration mode does not give a charge distribution across the activated pixels, instead gives either a one or zero. Therefore, a simple non-intensity weighted centroiding process in normal integration mode can produce similar results as utilizing a Gaussian fit for a charged activation area in pulse mode. The center of the activated area is found by dividing each pixel into sub-pixels (25 sub pixels per pixel in this case) and averaging through the area to find the center. An acquisition time of 180 seconds allowed for the ideal ratio of interacting neutrons without pixel overlapping events. Single neutron events can be observed within a single frame before individual bins are summed together in Figure 20. Each bin consists of ~1,000 frames summed together after individually being centroided, providing images for cold, thermal, and epithermal neutron energies or leave the individual 3197 bins for resonance analysis. Both methods are presented and the advantages are discussed.

<center>(a)   (b)   (c)</center>
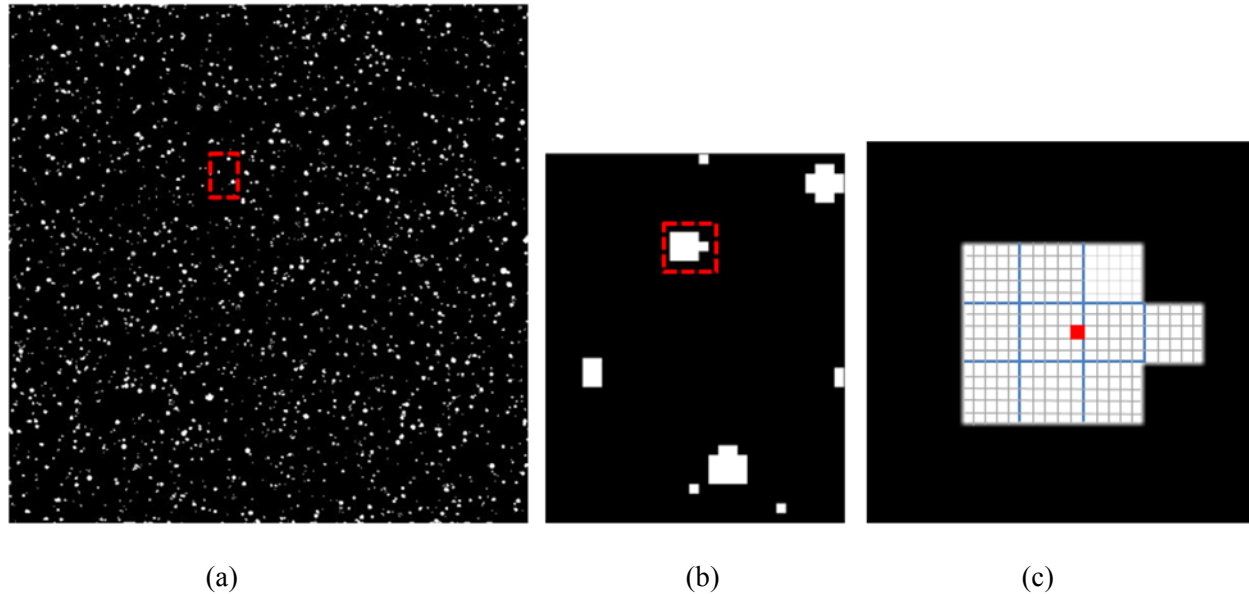
Figure 20: (a) Single neutron interaction frame (180 second acquisition time) for one energy bin (b) Zoomed in section of (a) marked by red dashed rectangle (c) Illustrated sub-pixel break down for a single neutron event marked by red dashed area in (b). One single 55 µm pixel is converted into a 5x5 subpixel array with sizes of 11 µm each. The red square indicates where the event will be centroided to a single sub pixel.

An open beam measurement to see the detector response with 12+ hours of acquisition time reveals the collimator hole array and allows for correction of patterns native in the detector. To confirm the presence of the collimator holes in the MCP, the fast Fourier transform was performed in Figure 21. The pattern in Figure 21b represents roughly 15 µm center to center holes in the collimator, whereas in Figure 21c the pattern is not present. This high resolution open beam can now be used for normalizing and correcting radiographs.
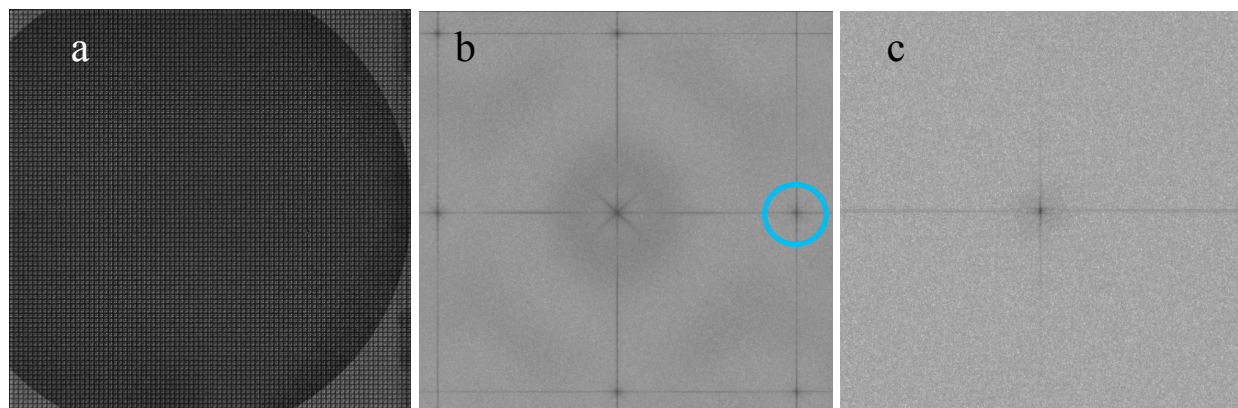
Figure 21: (a) Centroided image with 11 µm effective pixel size for cold neutron open beam radiograph (b) Fast Fourier transform showing artefact from centroiding and individual collimator pore size (blue). (c) Fast Fourier transform of non-centroided open beam demonstrating no effect from collimator hole size.

6.1.4   Increasing Spatial Resolution.

The PSI grating is an ideal standard for evaluating the overall resolution of an image. The frequency that line pairs are able to be resolved gives a direct correlation to the overall image resolution. The grating is

comprised of gadolinium regions of lines with widths of 160 µm, 80 µm, 40 µm, 20 µm, 10 µm, and 5 µm. Here the PSI grating was placed 42mm from the active detector area (30 mm from detector face and 12 mm from detector face to active area) and the image was acquired for 180 seconds and adding 44 individual images (total of 8,000 second exposures). A pre centroided image taken at Lujan center's flight path 5 beam line demonstrates the previous resolution limitation of the Medipix detector system. The smallest line that is resolved is the 80 µm level, as shown in Figure 22a. The fast Fourier transform (Figure 22b) converts the image into the frequency domain from the spatial domain and gives a better visual representation of the lines that can be resolved. The resolution can be calculated by finding the pixels/cycle and converting the size of the pixel to µm and dividing the cycle by two.
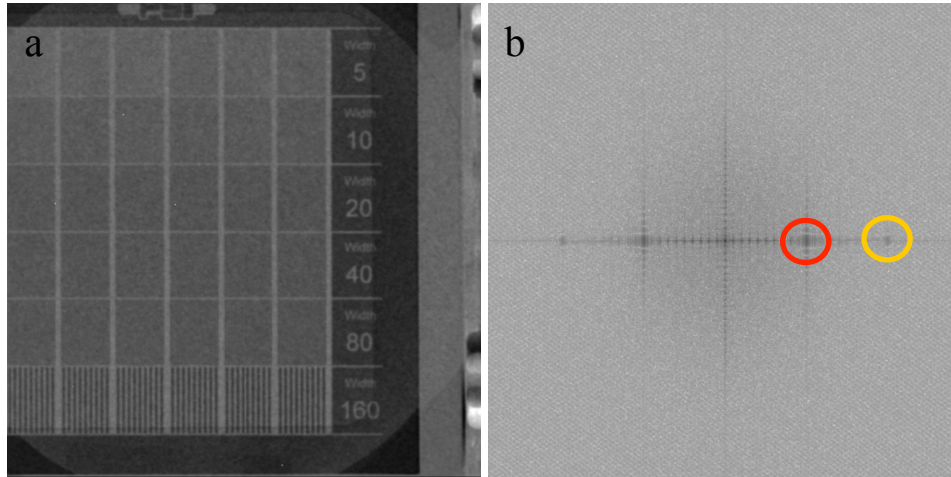
Figure 22: (a) Non-centroided image with 55 µm native pixel size for non energy resolved radiograph (b) Fast Fourier transform showing that 160µm, (red) and 80µm (orange) width line pairs are visible.

The non-centroided PSI grating was compared to the energy resolved centroided image as shown in Figure 23 and Figure 24. A cold neutron radiograph acquired for 8,000 seconds can resolve the 40µm width line pairs post-centroiding (Figure 23a). The fast Fourier transform (Figure 23b) demonstrates that the original pixel size of 55µm as an artefact but does not degrade the overall image. The thermal neutron energy radiograph (Figure 24a) can resolve down to the 40µm width line pairs. The contrast for thermal and epithermal neutrons suffers due to lower cross section of Gd for these energy ranges. Figure 25 compares the entire non centroided spectrum to that of the entire centroided spectrum with no energy resolution.
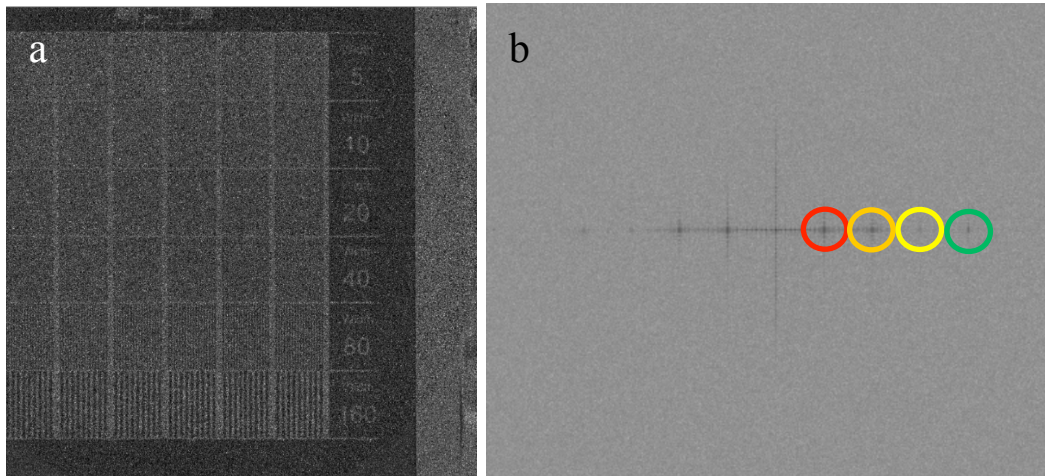
Figure 23: (a) Centroided image with 11 µm effective pixel size for cold energy resolved neutrons (6meV) (b) Fast Fourier transform showing 160 µm (red), 80µm (orange), and 40µm(green) width line pairs are visible. The yellow represents the original 55 µm pixel resolution.
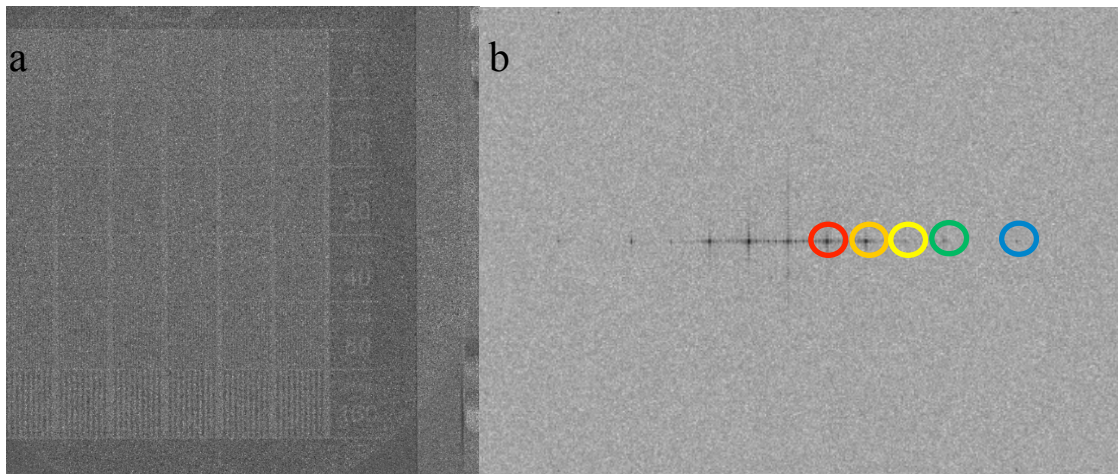
Figure 24: (a) Centroided image with 11 µm effective pixel size for thermal energy resolved neutrons (25meV) (b) Fast Fourier transform showing 160µm (red), 80µm (orange), and 40µm (green) width line pairs are visible. Yellow represents the original 55 µm resolution and blue is the 11 µm collimator holes.
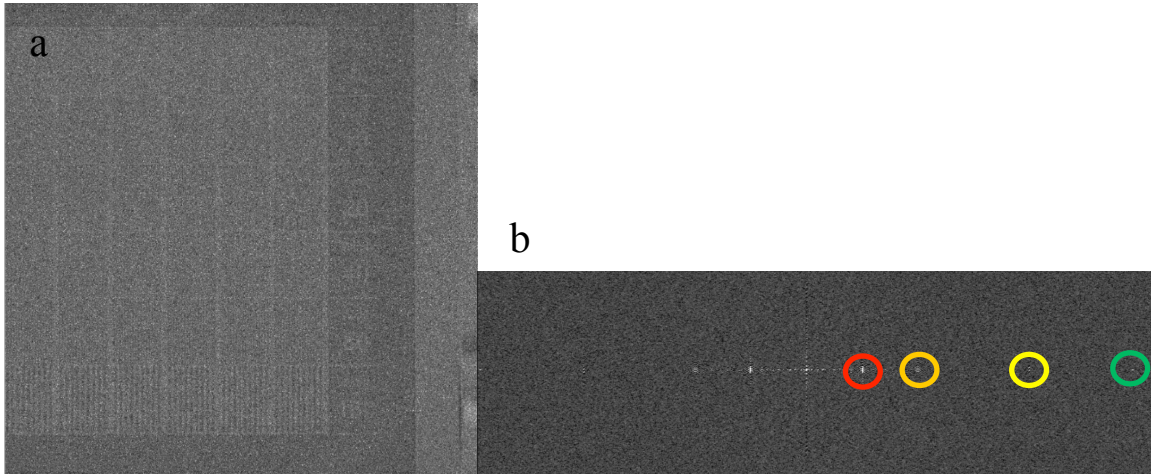
Figure 25: (a) Centroided image with 11 µm effective pixel size for entire energy resolved region. (b) Fast Fourier transform showing 160 µm width line pairs (red), 80 µm width line pairs (orange), and 40 µm width line pairs (green). Yellow represents the original 55 µm resolution.

The highest possible resolution of the system, assuming perfect counting statistics, can be found by taking the modulation transfer function (MTF) at 10% of a slant edge function. The ASTM E545 provides information on beam and image quality by imaging a lead disk, boron nitride disk, and a cadmium wire setup [52]. The construction of the imaging standard is shown in Figure 26.
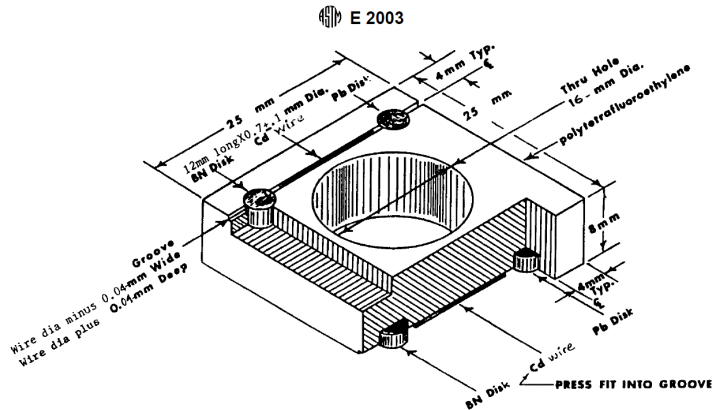
Figure 26: ASTM E 2003 standard purchased from NRAY services consisting of polytetrafluoroethylene, 99.9% cadmium, 99.9% lead, and 40% elemental boron nitride.

The MTF of an imaging system is defined by the absolute value of its optical transfer function and is limited at the high end by the Nyquist frequency [53]. The limiting spatial resolution is considered to be when the MTF crosses 10% due to a single sinusoidal wave needs two adjacent pixels to display a full cycle. The Nyquist frequency is then always 0.5 cycles per pixel (or twice the size of one pixel). To obtain the MTF, the cadmium wire provides an edge to produce and edge spread function. The edge spread function is then differentiated to obtain the line spread function. The MTF is then calculated by taking the Fourier transform of the line spread function. The standard non centroided and energy resolved centroided radiographs are shown in Figure 27. The processed radiographs confirm a resolution in agreement with the determination with the PSI grating. The MTF at 10% shows that the resolution can be further increased with better statistics and sample positioning.
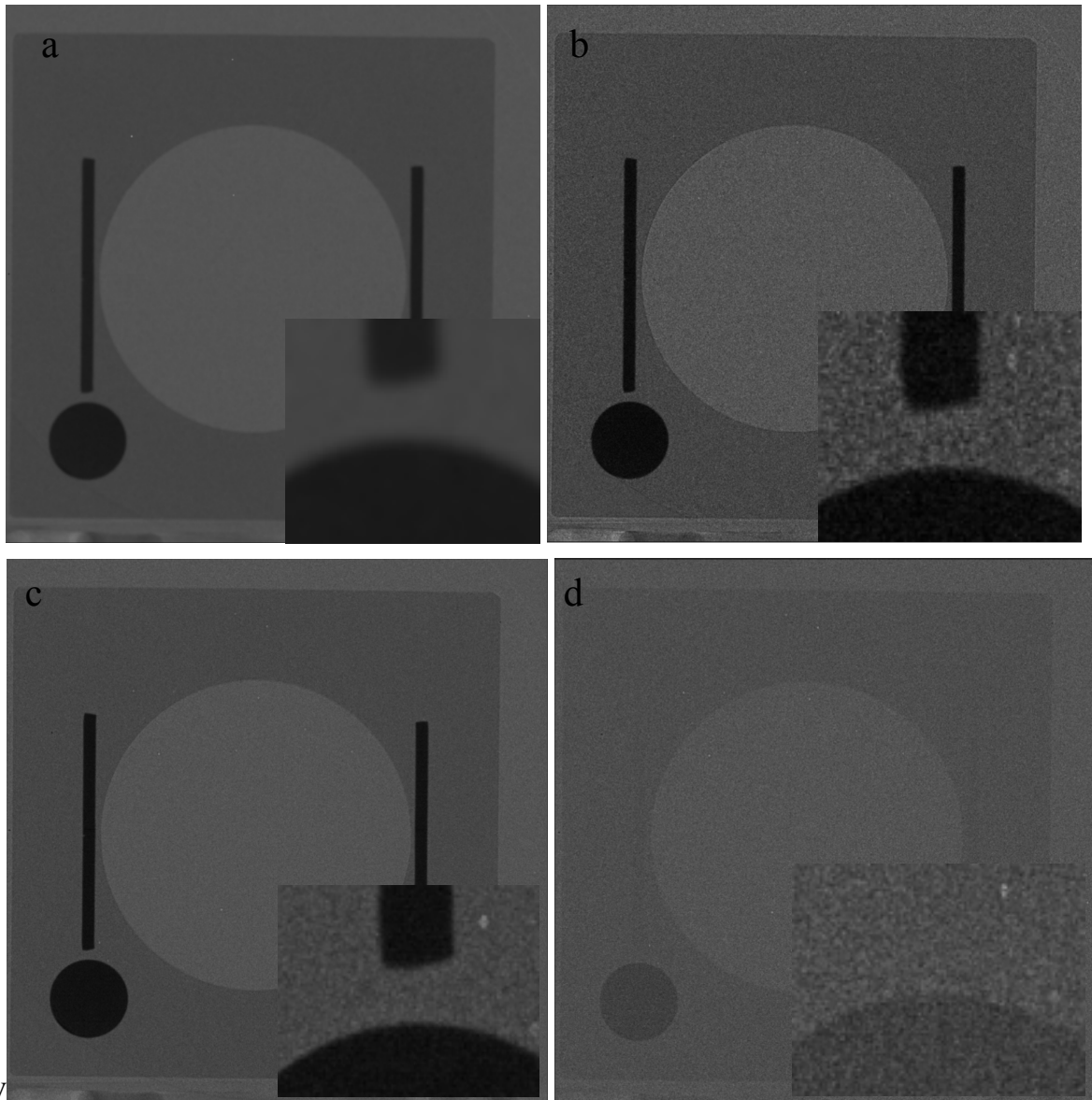
Figure 27: (a) Non-centroided image with original 55 μm pixel size. Imaging ASTM beam purity standard with entire spectrum of neutrons with ~80 μm resolution. Bottom right corner enhanced to show the opaque disk's edge resolution. (b) Centroided image with 11 μm effective pixel size and with ~40 μm spatial resolution using cold neutrons. (c) Centroided image with 11 μm effective pixel size and with ~40 μm spatial resolution using thermal neutrons. (d) Centroided image with 11 μm effective pixel size and with ~40 μm spatial resolution. The cadmium wire at this energy is almost completely transparent signifying a resonance peak.

The MTF is plotted vs spatial frequency for the ASTM standard radiographs (Figure 28). To obtain resolution in μm, cycles/pixel must be converted to line pairs/mm first by using the pixel pitch size. The resolution can now be found by converting line pairs/mm to μm at 10% on the MTF curve. The non-centroided radiograph results in the highest possible resolution of 70 μm, which can be confirmed in the PSI grating where the 80 μm width pairs can barely be resolved. The cold neutron energy centroided region results in a resolution of 29 μm and the thermal region results in 22 μm. This cannot be any higher at this point due to the Nyquist frequency being the size of two pixels, or 22 μm. Epithermal resolution was not calculated due to low statistics and could not calculate an edge spread function.
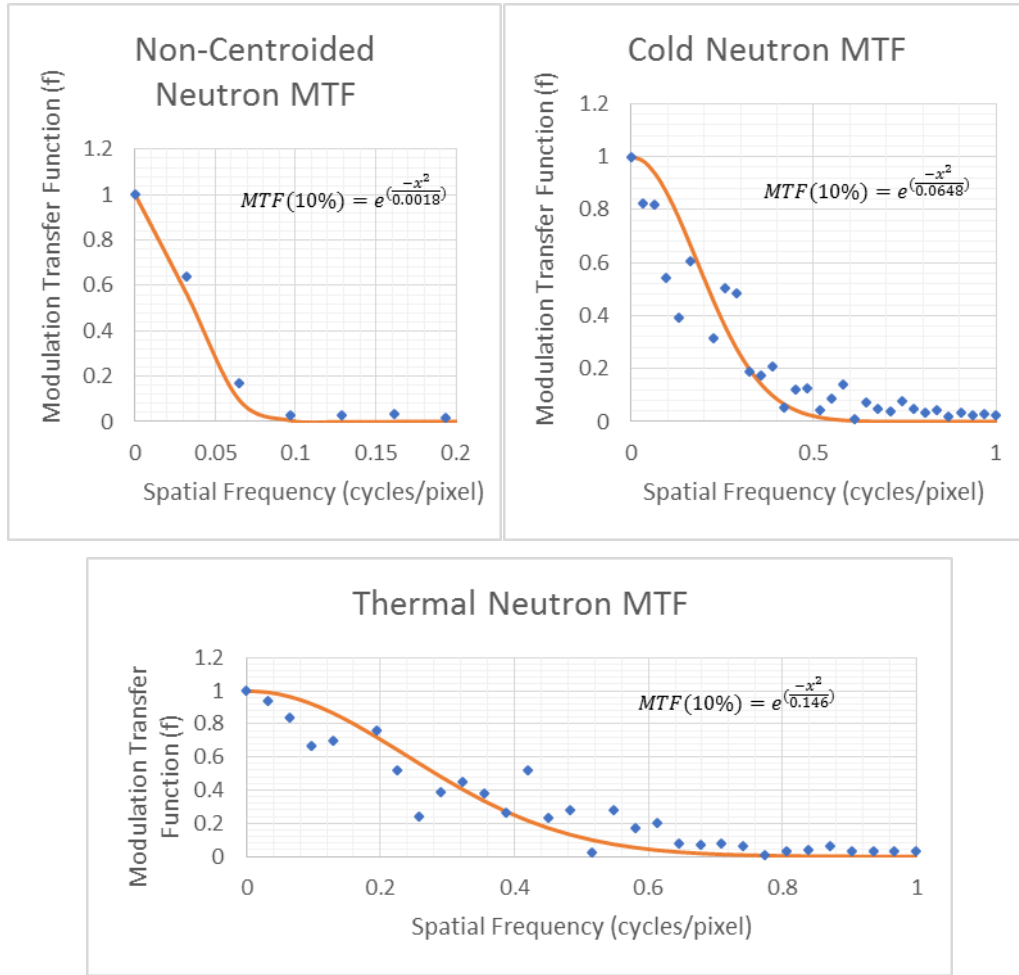
Figure 28: Modulation Transfer Function plots for non centroided, centroided cold and thermal radiographs.

6.1.5   Future Development

Imaging with higher number of subpixels will allow the Nyquist frequency limit to go down and provide higher resolution images. This process can be applied by imaging a full centroided tomography with the entire energy spectrum. The next step is imaging nuclear fuel pellets with ~20 μm resolution and with isotope quantification. About 3 GB of data is created every minute and faster and larger hard drives are required to keep the acquisition and processing time low.

6.2   High-rate Liquid Scintillator Detector

Flight-path 5 is equipped with two detector stations: The main cave, utilized here and several previous reports and allowing source-detector distances from ~6.5 to 11.5 m (the "cave"), but also a second long-distance detector station (the "silo") with detector distances from ~58 to 62 m. The time-of-flight resolution for resonance measurements at this second station is superior due to the $\Delta L/L$ term (with ΔL being typically dominated by the moderator thickness and L being the source to detector distance). For imaging applications, this station offers superior L/D (with D being the smallest beam diameter and L the distance between that point and the sample) ratios as well as a beam spot that can cover >0.5 m for thermal radiography. The high-rate detector was recently installed in the 60m silo station. A schematic of

the dimensions and detector layout is shown in Figure 29. In the context of the NE mission, the superior energy resolution from the longer flightpath length and increase detector efficiency (see below) can be utilized to gain further insight on the material by detailed analysis of the resonance profile to gain further insight on the material, in particular at non-ambient conditions such as high temperature during sintering. Using the combination of the imaging detector in the cave to e.g. move a certain sample volume with a feature of interest into a neutron beam collimated to a small (e.g. 1mm) diameter beam would allow characterizing that feature with the high-rate detector in the silo to add detail to the characterization by energy-resolved imaging in the cave. Furthermore, the difference in neutron conversion to light from the [10]B loaded glass in the mm thick MCP of the imaging detector to the liquid scintillator of several cm in the high-rate detector increase the efficiency significantly.
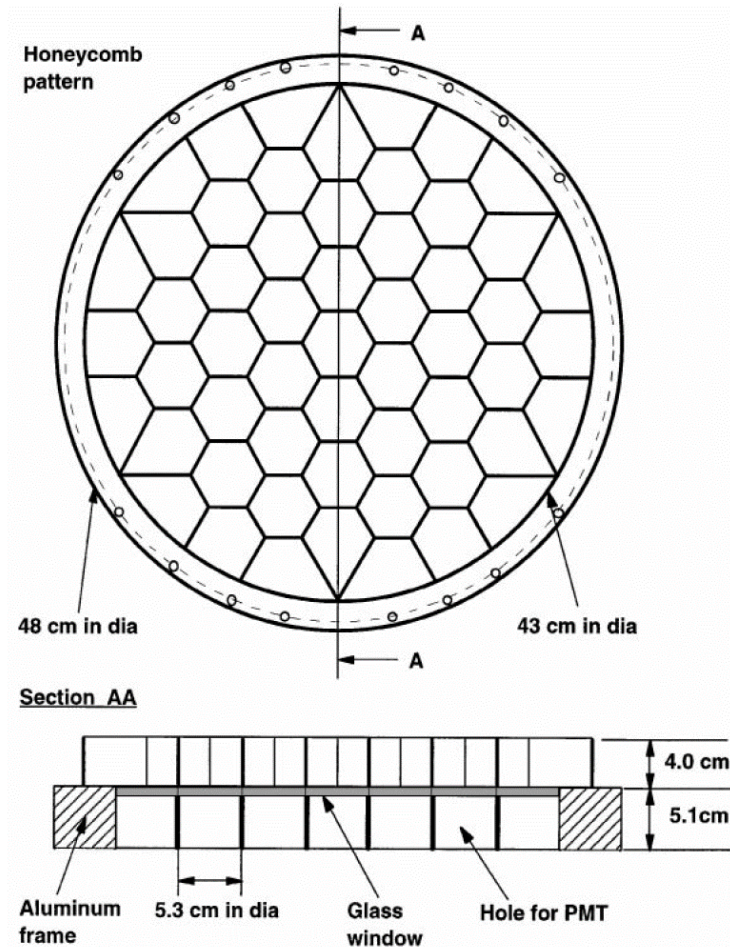
Figure 29: The 55-module 10B-loaded liquid scintillation detector. The upper part of the figure shows the honeycomb pattern of the liquid scintillator cell arrangement. Each cell is viewed by a 5-cm diameter photomultiplier tube. The lower part of the figure shows the cross sectional view of the scintillation container without the aluminium entry window flange (from [47]).

The efficiency values reported by Yen et al [47] are 95%, 85%, 71% for 10, 100, 1000 eV neutron energies. This is far superior to the efficiency of the MCP glass, that is quoted as 50% and 70% at 25 meV (thermal neutrons) and 5 meV (cold neutrons) [9]. For epi-thermal neutrons, the MCP efficiency is in the percent range and essentially zero for keV neutrons. Having a larger neutron energy available, selected regions of a sample could be aligned within a small neutron beam with the imaging detector after bulk characterization with the regular ~1 inch diameter beam and then characterized with neutron resonance analysis of superior quality.

The setup requires 55 high-voltage channels and the same number of digitizers. While the high voltage power supplies are located next to the detector, 55 signal cables reach from the bottom of the silo ~10m up to the hutch where the data acquisition electronics are located. All 55 detector channels were tested with a radioactive gamma source and 53 were made operational. During initial tests with spallation neutron pulses, six of the 55 photomultiplier tubes were operated, producing the data shown in Figure 30. The resonance observed at ~60 μs corresponds to a neutron energy of ~500 eV, illustrating the greatly extended energy range accessible with the detector. Note that the detector is not properly calibrated at this time and the data shown below is raw data, i.e. neither normalized nor background corrected, which are forthcoming activities.
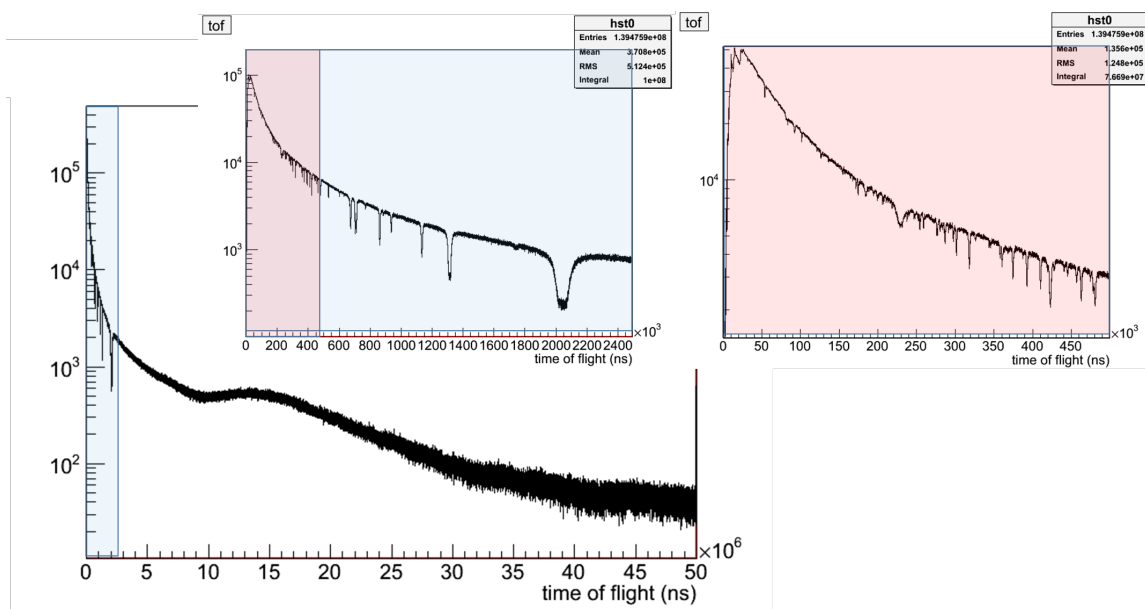
Figure 30: Neutron intensities measured as a function of time-of-flight over the duration of one of the 50 ms/20 Hz pulses. The sample was one of the dU fuel rods discussed in this report with a Ta sheet as internal standard. The shaded areas in the figures are zoomed in the insets. The neutron energies corresponding to the maximum time-of-flight in each graph are 7 meV/50 ms, 2.8 eV/2.5 ms, and 70.3 eV/500 μs.

7.   Discussion

The entire volumes of two 156 mm long, 11mm diameter irradiation capsules, with stacks of 102 mm high composite ceramic nuclear fuel were characterized with several neutron based methods. Neutrons readily penetrate the double-walled steel containment and allow directly characterizing the bulk of the depleted uranium fuels.

Imaging of the capsules reveals the integrity of the fuel within the cladding. Due to difficulties in the FY16/17 run-cycle, only a qualitative image analysis is provided in this report. Current data collection for a higher spatial resolved data set is in progress. The spatial resolution for previous measurements was limited to about 100 μm for tomographic reconstruction. However, current data-acquisition is ongoing using pixel centroiding to improve spatial resolution up to 22 μm. This would allow to better resolve the cladding to fuel gap. Additionally to the improved spatial resolution, a liquid scintillator based detector was deployed running congruently to the pixelated TOF detector at the 60 m flight-path station at FP5. This detector provides a high efficiency for up to keV neutrons, enabling the observation of isotopes with resonances that cannot be resolved with the pixelated TOF detector positioned at ~10 m.

From the diffraction data analysis, weight fractions, lattice parameters, and texture of the two steel phases of the two container materials as well as the two phases in the fuel were measured independently. The analysis of the weight fraction data did not show any trends or clustering, indicating that the samples are homogeneous with respect to their phase composition. For the lattice parameter analysis, one of the steel phases (austenite) was used as an internal standard, while the second steel phase and the UN phase did not show significant variations. The crystal lattice of the U_3Si_5 exhibits some clustering. The lattice parameter of this phase is sensitive to the chemistry, in particular possible absorption of nitrogen atoms into the U_3Si_5 crystal lattice. This can occur during the melting and resolidification during the sintering occurring at close proximity to the melting point of U_3Si_5. Small temperature variations in the furnace could then explain differences between pellets. Further research on the effect of dissolution of UN in the presence of U_3Si_5 melt and nitrogen incorporation in the U_3Si_5 crystal lattice would be required to allow a better interpretation of this effect. The pole figures, describing the preferred orientation within each phase, also show slight variations in the U_3Si_5 results, supporting that the observed inhomogeneities predominantly exist in U_3Si_5. This phase is anisotropic with a hexagonal crystal structure. While macroscopic thermal properties were derived [35], the anisotropy of the thermal expansion along the crystallographic *a* and *c* axes is to the best of our knowledge unknown. Presence of larger single crystalline volumes in the matrix, as indicated by stronger pole figure maxima in the *c* axis pole figures (001 pole figures above), could amplify anisotropic thermal expansion which ultimately could lead to failure. Mechanical modeling, using for instance self-consistent models, could allow calculating the magnitude of the mechanical stresses induced during cooling by >1700°C or during re-heating.

The present report adds another data set to pre-irradiation characterization. Having such data available on pellets which actually will be irradiated might allow interpreting failure (e.g. due to the slight variations in preferred orientation and U_3Si_5 lattice parameters, indicating chemistry changes). Measuring the same specimen again after irradiation would provide the first detailed bulk pre- and post-irradiation characterization, which would accelerate insight gained from irradiation tests. The national capacity for destructive PIE of irradiated fuels is limited. The cost is large and the schedule constrained. For these reasons there is merit in exploring the opportunity to non-destructively examine the entire bulk irradiated fuels with methods presented here. At the current point in development of the neutron-based techniques they have the potential to contribute mechanical integrity, phase, isotopic distribution and pellet clad interactions data for many cubic centimeters of irradiated fuel that is integral to validation of mesoscale/engineering scale models. Improved spatial resolution is a key development goal. However the shipping cost for moving irradiated fuels between INL and LANL remains an impediment. One exciting possibility that is under consideration concerns the availability of nascent neutron production technologies using small-scale accelerator and laser based sources that might be realized to enable poolside characterization at INL or industrial facilities.

8.   Future Work

Tomographic analysis

Data analysis of the energy-resolved neutron imaging data, i.e. processing of hundreds of thousands or even millions of data sets with SAMMY analysis, poses challenges in data handling, but also in assessment of the quality of each fit. Our group continuously develops tools to facilitate this analysis. Assessment of the error bars produced by the SAMMY code for areal densities and the potential inclusion of these errors for error propagation into the CT algorithms is an on-going effort.

Improved Spatial Resolution from Pixel Centroiding

The pixel centroiding demonstrated in this report is in the process of becoming part of standard imaging procedures. The data volume is increased by about an order of magnitude, reaching ~1.5 TB per tomography dataset. We are exploring multi-CPU real time processing to address this problem as well as

upgraded data storage infra-structure. A full CT test, translating the improved 2D resolution into 3D resolution, is also on-going at the time of this report.

Improved Experimental procedure

Actinide samples create significant prompt gamma background as well as self attenuation of the neutron beam, thus the single tantalum foil used as a standard does not fulfill the assumption in the SAMMY model that the measured transmission data is a homogeneous mixture within the sample volume. To draw the calibration closer to the assumption we will investigate whether a configuration in which two tantalum foils, one in front and one behind the sample volume improves the background determination. Scatter rejection, realized by installation of multi-channel plates between sample and detector, allowing only transmitted neutrons to reach the detector but rejecting secondary radiation emitted from the source, are also explored in a collaboration with Worcester Polytechnic Institute.

Improved background to provide access to higher energy resonances.

Resonances in these studies have been measured up to 200eV before the signal to noise precluded further measurements. However the same detector employed at the J-PARC pulsed neutron source in Japan observed resonances up to keV [46]. Thus mitigating the instrument background on FP-5 is a key goal to expand the energy range over which isotopic resonances can be measured.

Configuration changes reducing the air scatter, e.g. with flight tubes and more shielding along the flight path, have not reduced the background. It is therefore determined that the background present in the data is predominantly originating in the spallation target/moderator/reflector system, which emits neutrons arriving at time-of-flights that do not correspond to their energies. One source of this effect could be inelastic scattering from surfaces on the inner diameter of the collimator rings. Installation of beam scrapers, made from borated steel (NEUTRONIT from Boehler, Austria), could mitigate the direct view of the detector on these surfaces. Finally, the shape of the entrance and exit collimation will be modified to better match the shape and dimensions of the moderator and detector (after an approach demonstrated at FRM-2 in Europe). Another background component originates from the moderator on the opposite side of the target/moderator/reflector assembly. Discussion as to whether this background can be reduced during the on-going target re-design of the LANSCE target-1 are on-going and the LANL team is a key contributor.

Improved imaging detector technology

Currently the detector used in these measurements employs a boron and gadolinium-doped MCP. It was developed for use in the thermal regime for which the Gd epithermal resonances response were irrelevant but which complicate measurements in the 1 to 200eV range. An effort will be pursued to explore the option of a boron-only MCP for the detector. Initial discussion with Bruce Feller of Nova Scientific, manufacturer of the boron doped MCPs, indicate that even higher boron concentrations could be feasible.

Diffraction analysis
Diffraction measurements of stoichiometry and phase were performed using the HIPPO instrument. The simple Cd slit does not provide flexibility to for the probed volume. A full boron-nitride based collimation slit system was developed over the summer and awaits commissioning on the HIPPO beam line. This slit package will allow horizontal slits in <0.1 mm increments as well as vertical slits, thus allowing further reduction of the probed volume to characterize regions of interest identified with larger probed volumes. To provide data to understand the mechanical stresses induced by anisotropic thermal expansion, measurements of the crystal structure evolution of U_3Si_5 and other U-Si phases are planned in the on-going run cycle.

Continued assessment of potential for study of irradiated fuels
The measurements on the pre-irradiated material are valuable in their own right but a huge "payoff" for this work would be to perform measurements on irradiated fuel rodlets. The fuels campaign is

specifically holding back MOX and MA-MOX rodlets irradiated in the AFC-2C test from traditional PIE with the intent of performing the ANDE with methods described in this report. Demonstration of the viability of measurements on irradiated fuel by a detector test performed by Anton Tremsin at INL in May 2016 demonstrated satisfactory detector performance in the vicinity of irradiated fuel, demonstrating the ability of the detector type used in this report to resolve the neutron measurements from the gamma induced signal from real irradiated fuels. Appendix A section 11 of a previous report [11] includes a conceptual cask for handling rodlets of LANL ATF in the beam line. Discussion about handling irradiated fuel rodlets and hot cell utilization at LANL, in particular within the framework of the recent partner status of LANL with the NSUF, are ongoing.

High energy resolution measurements with the ^{10}B liquid scintillator detector
The recently installed high rate ^{10}B liquid scintillator detector, located in the 60 m station, is in the process to become fully operational (i.e. all 55 instead of six detector channels, calibration etc.). This detector will improve the efficiency at higher neutron energies compared to the imaging detector as well as improve the energy resolution due to the longer flightpath length. With a smaller collimation (mm sized instead of cm sized) this will allow interrogation of regions of interest identified with the imaging setup and aligned in the beam with the motion control equipment of the imaging beam line, providing a unique advantage of a combined material science/radiography and nuclear physics setup for enhanced material characterization. Applying this detector to study the influence of the chemical environment of the absorbing nucleus, i.e. the ^{238}U resonance measured in metallic uranium, UO_{2+x}, UN, U_3Si_5, is a high priority. Furthermore, temperature measurements by resonance Doppler broadening are scheduled for in situ measurements.

Continued engagement in development of laser-driven neutron sources

The possibility of bring the neutron characterization capability poolside to storage facilities may be enabled in the future by laser drive neutron sources [3]. To this end, LANL is organizing a workshop bringing together world-leading experts in laser design, particle acceleration with lasers, neutron production with lasers and conventional methods as well as communities benefitting from these developments. The LANL team is engaged in discussions to define the boundary conditions as well as timelines for potential deployment of such a source at INL.

9.   Conclusions
Between November 2016 and January 2017 as well as in August 2017, energy resolved neutron imaging data as well as diffraction data were collected on mock-up accident tolerant fuels with $UN-U_3Si_5$ composite composition. The entire ~10 cm long, ~1 cm diameter fuel volume could be characterized, however due to time constraints only 2 mm slices in 4mm increments were characterized with neutron diffraction and a 28mm subset of the entire sample was characterized with energy-resolved neutron imaging. The double encapsulation of the fuel into two steel containers does not pose a problem for the neutron analysis and the methods could be applied to enriched (demonstrated previously, e.g. [11]) as well irradiated fuels.

Both approaches, imaging and diffraction, indicate that the fuel pellets are homogeneous. Slight deviations from the homogeneity were observed in the U_3Si_5 by diffraction. The observed changes are consistent with melting and resolidification of larger volumes of U_3Si_5 (texture) which may absorb some UN, leading to lattice parameter changes.

The energy-resolved neutron imaging developed at LANL has matured to a state where the accuracy and precision of the partial densities of isotopes is in excellent agreement with the partial densities determined by mass spectrometry [54]. In combination with access to epi-thermal neutrons for a reliable tomographic reconstruction of the sample shape, and spatially resolved isotope density measurements with ~55 μm resolution, a potentially powerful tool for fuel characterization has emerged. Neutron diffraction, albeit

potentially not probing the entire sample in the case of higher enriched fuels, can complement this information with microstructural information.

The application of non-destructive neutron based evaluation for the analysis of as-fabricated nuclear fuels has the potential to provide critical enabling data to realize science based fuels development. For R&D research on small batches of prototype material it maximizes the scientific merit of irradiations by establishing the initial condition of the material as well as serving a Quality Assurance role. By characterizing fuels before irradiation it can identify features that are invisible to visual inspection which may or may not be a cause for rejecting a pellet. Non-destructive characterization of irradiated material has the potential to ensure that destructive evaluation in hot cells is used to maximum cost efficiency by directing focus to regions in samples that represent average and or atypical behavior.

Neutron tomographic imaging and scattering measurements on nuclear fuels of fabrication geometries provide non-destructive measurement of cracks, flaws, chemistry, phase, texture, and fission gas pressure. The data for fresh fuel contributes data that establishes the benchmark for the initial condition of the fuel. Measurements on irradiated fuel could add substantial data sets for validating the modeling and simulation of irradiation effects that are integral to improved fuel performance codes.

10. References

[1] M.D. Roth et al. "Bright laser-driven neutron source based on the relativistic transparency of solids." Physical review letters 110, no. 4 (2013): 044802.

[2] Fernández, J. C., Cort Gautier, D., Huang, C., Palaniyappan, S., Albright, B. J., Bang, W., ... & Roth, M. (2017). Laser-plasmas in the relativistic-transparency regime: Science and applications. Physics of Plasmas, 24(5), 056702.

[3] M. Roth, S. C. Vogel, M. A. M. Bourke, J. Fernandez, M. Mocko, S. Glenzer, W. Leemans, C.W. Siders, C. Haefner, "Assessment of Laser-Driven Pulsed Neutron Sources for Poolside Neutron-based Advanced NDE – A Pathway to LANSCE-like Characterization at INL", Report NTRD-FUEL-2017-000064 to DOE/NE, LA-UR-17-23190 (2017).

[4] C. Morris, M. Bourke, D. Byler, C. Chen, G. Hogan, J. Hunter, K. Kwiatkowski, F. Mariam, K. McClellan, F. Merrill, et al., "Qualitative comparison of bremsstrahlung X-rays and 800 MeV protons for tomography of urania fuel pellets", Review of Scientific Instruments 84 (2013) 023902.

[5] M. B. Aufderheide III, H.-S. Park, E. P. Hartouni, P. D. Barnes, D. M. Wright, R. M. Bionta, J. D. Zumbro, C. L. Morris, "Proton radiography as a means of material characterization", AIP Conference Proceedings, 497 (1999) 706.

[6] Brown, D. W., Okuniewski, M. A., Almer, J. D., Balogh, L., Clausen, B., Okasinski, J. S., & Rabin, B. H. (2013). High energy X-ray diffraction measurement of residual stresses in a monolithic aluminum clad uranium–10wt% molybdenum fuel plate assembly. Journal of Nuclear Materials, 441(1), 252-261.

[7] AS Tremsin, JB McPhate, JV Vallerga, OHW Siegmund, JS Hull, WB Feller, and E Lehmann. High-resolution neutron radiography with microchannel plates: Proof-of-principle experiments at psi. Nuclear Instruments and Methods in Physics Research Section A: Accelerators, Spectrometers, Detectors and Associated Equipment, 605(1):103–106, 2009.

[8] Vogel et al., "Assessment of advanced NDE techniques and the path forward to evaluating an AFC-2 irradiated fuel pin", LA-UR 13-2167.

[9] A. Tremsin, S. Vogel, M. Mocko, M. Bourke, V. Yuan, R. Nelson, D. Brown, B. Feller, "Non-destructive studies of fuel rodlets by neutron resonance absorption radiography and thermal neutron radiography", Journal of Nuclear Materials, 440 (2013) 633–646.

[10] Bourke, M. A., Vogel, S. C., Voit, S. L., Mcclellan, K. J., Losko, A. S., & Tremsin, A. (2016). Non destructive examination of UN/U-Si fuel pellets using neutrons (preliminary assessment) (No. LA-UR--16-22179). Los Alamos National Lab.(LANL), Los Alamos, NM (United States).

[11] Sven C. Vogel, Adrian S. Losko, Reeju Pokharel, Timothy L Ickes, James Hunter, Donald W. Brown, Stewart L. Voit, Anton S. Tremsin, Mark A.M. Bourke, Kenneth J. McClellan, "Non-destructive Pre-irradiation Assessment of UN / U-Si "LANL1" ATF formulation", Report to DOE/NE, LA-UR-16-27110 (2016).

[12] Tremsin, A. S., Losko, A. S., Vogel, S. C., Byler, D. D., McClellan, K. J., Bourke, M. A. M., & Vallerga, J. V. (2017). Non-contact measurement of partial gas pressure and distribution of elemental composition using energy-resolved neutron imaging. AIP Advances, 7(1), 015315.

[13] Vogel, S. C., Bourke, M. A., & Losko, A. S. (2016). Neutron based evaluation in support of NEAMS (No. LA-UR--16-23977). Los Alamos National Lab.(LANL), Los Alamos, NM (United States).

[14] Vogel, S. C. (2013). A review of neutron scattering applications to nuclear materials. ISRN Materials Science, 2013.

[15] Hellenbrandt, M. (2004). The inorganic crystal structure database (ICSD)—present and future. Crystallography Reviews, 10(1), 17-22.

[16] EH Lehmann, G Frei, P Vontobel, L Josic, N Kardjilov, A Hilger, W Kockelmann, and Axel Steuwer. The energy-selective option in neutron imaging. Nuclear Instruments and Methods in Physics Research Section A: Accelerators, Spectrometers, Detectors and Associated Equipment, 603(3):429–438, 2009.

[17] Michael Schulz, Peter Böni, Elbio Calzada, Martin Mühlbauer, and Burkhard Schillinger. Energy-dependent neutron imaging with a double crystal monochromator at the ANTARES facility at FRM II. Nuclear Instruments and Methods in Physics Research Section A: Accelerators, Spectrometers, Detectors and Associated Equipment, 605(1):33–35, 2009.

[18] M Strobl, I Manke, N Kardjilov, A Hilger, M Dawson, and J Banhart. Advances in neutron radiography and tomography. Journal of Physics D: Applied Physics, 42(24):243001, 2009.

[19] Messaoudil, C., Boudier, T., Sorzano, C. O. S., & Marco, S. (2007). TomoJ: tomography software for three-dimensional reconstruction in transmission electron microscopy. BMC bioinformatics, 8(1), 288.

[20] Schneider, C. A., Rasband, W. S., & Eliceiri, K. W. (2012). NIH Image to ImageJ: 25 years of image analysis. Nature methods, 9(7), 671-675.

[21] MB Chadwick, M Herman, P Oblozinsky, Michael E Dunn, Y Danon, AC Kahler, Donald L Smith, B Pritychenko, Goran Arbanas, R Arcilla, et al. ENDF/B-VII. 1 nuclear data for science and technology: cross sections, covariances, fission product yields and decay data. Nuclear Data Sheets, 112(12):2887–2996, 2011.

[22] http://web.ornl.gov/sci/nuclear_science_technology/nuclear_data/sammy/

[23] Philip G Burke and Keith A Berrington. Atomic and molecular processes: an r-matrix approach. 1993.

[24] N. Larson, "Updated user's guide for SAMMY: multilevel R-matrix fits to neutron data using Baye's equations." No. ORNL/TM-9179. Oak Ridge National Lab., TN (USA), 1984.

[25] M. Mocko et al., "Advantages and limitations of nuclear physics experiments at an ISIS-class spallation neutron source." Nuclear Instruments and Methods in Physics Research Section A: Accelerators, Spectrometers, Detectors and Associated Equipment 589.3 (2008): 455-464.

[26] Larson, Allen C., and Robert B. Von Dreele. "Gsas." General Structure Analysis System. LANSCE, MS-H805, Los Alamos, New Mexico (1994).

[27] Vogel, Sven C. "gsaslanguage: a GSAS script language for automated Rietveld refinements of diffraction data." Journal of Applied Crystallography 44, no. 4 (2011): 873-877.

[28] Lutterotti, L., S. Matthies, H-R. Wenk, A. S. Schultz, and J. W. Richardson Jr. "Combined texture and structure analysis of deformed limestone from time-of-flight neutron diffraction spectra." Journal of Applied Physics 81, no. 2 (1997): 594-600.

[29] Rietveld, H. M. "A profile refinement method for nuclear and magnetic structures." Journal of applied Crystallography 2, no. 2 (1969): 65-71.

[30]   Von Dreele, R. B. "Quantitative texture analysis by Rietveld refinement." Journal of Applied Crystallography 30, no. 4 (1997): 517-525.

[31]   Wenk, H. R., Lutterotti, L., & Vogel, S. (2003). Texture analysis with the new HIPPO TOF diffractometer. Nuclear Instruments and Methods in Physics Research Section A: Accelerators, Spectrometers, Detectors and Associated Equipment, 515(3), 575-588.

[32]   Losko, A. S., Vogel, S. C., Reiche, H. M., & Nakotte, H. (2014). A six-axis robotic sample changer for high-throughput neutron powder diffraction and texture measurements. Journal of Applied Crystallography, 47(6), 2109-2112.

[33]   Wenk, H-R., L. Lutterotti, and S. C. Vogel. "Rietveld texture analysis from TOF neutron diffraction data." Powder Diffraction 25, no. 3 (2010): 283-296.

[34]   S.L. Voit, J.T. White, D.D. Byler, J.T. Dunwoody, P. Medvedev, P. Glass, A.T. Nelson, and K.J. McClellan, Fabrication of Accident Tolerant U-Si Fuel Forms. Proceedings of Top Fuel 2016: LWR Fuels with Enhanced Safety and Performance, Boise Idaho, USA. September 11-16, 2016. 1357-1366.

[35]   White, J., Nelson, A., Byler, D., Safarik, D., Dunwoody, K., McClellan, K., "Thermophysical Properties of U_3Si_5 to 1773K", J. Nucl. Mater., 456, 442-448, (2015).

[36]   Kohler, T. (2004, October). A projection access scheme for iterative reconstruction based on the golden section. In Nuclear Science Symposium Conference Record, 2004 IEEE (Vol. 6, pp. 3961-3965). IEEE.

[37]   Kaestner, A., Münch, B., Trtik, P., & Butler, L. (2011). Spatiotemporal computed tomography of dynamic processes. Optical Engineering, 50(12), 123201-123201.

[38]   Priesmeyer, H. G., & Harz, U. (1976). Isotopic assay in irradiated fuel by neutron resonance analysis. Safeguarding nuclear materials, 20-24.

[39]   Sterbentz, J. W., & Chichester, D. L. (2010). Neutron resonance transmission analysis (NRTA): a nondestructive assay technique for the next generation safeguards initiative's plutonium assay challenge (No. INL/EXT-10-20620). Idaho National Laboratory (INL).

[40]   Chichester, D. L., & Sterbentz, J. W. (2011, July). A second look at neutron resonance transmission analysis as a spent fuel NDA technique. In Conference: INMM 52nd Annual Meeting, Palm Desert, CA USA,< http://www. inl. gov/technicalpublications/Documents/4953376. pdf.

[41]   Chichester, D. L., & Sterbentz, J. W. (2011). Neutron resonance transmission analysis (NRTA): initial studies of a method for assaying plutonium in spent fuel (No. INL/CON-10-20684). Idaho National Laboratory (INL).

[42]   Neutron News, Vol. 3, No. 3, 1992, pp. 29-37

[43]   Carmack, W. J., Porter, D. L., Chang, Y. I., Hayes, S. L., Meyer, M. K., Burkes, D. E., ... & Somers, J. (2009). Metallic fuels for advanced reactors. Journal of Nuclear Materials, 392(2), 139-150.

[44]   Janney, D. E., Kennedy, J. R., Madden, J. W., & O'Holleran, T. P. (2015). Am phases in the matrix of a U–Pu–Zr alloy with Np, Am, and rare-earth elements. Journal of Nuclear Materials, 456, 46-53.

[45]   Janney, D. E., & Papesch, C. A. (2015). FCRD Transmutation Fuels Handbook 2015 (No. INL/EXT--15-36520). Idaho National Laboratory (INL), Idaho Falls, ID (United States).

[46]   A. Tremsin, private communication.

[47] Yen, Yi-Fen, J. D. Bowman, R. D. Bolton, B. E. Crawford, P. P. J. Delheij, G. W. Hart, T. Haseyama et al. "A high-rate 10 B-loaded liquid scintillation detector for parity-violation studies in neutron resonances." Nuclear Instruments and Methods in Physics Research Section A: Accelerators, Spectrometers, Detectors and Associated Equipment 447, no. 3 (2000): 476-489.

[48] Tremsin, Anton S., Jason B. McPhate, John V. Vallerga, Oswald HW Siegmund, W. Bruce Feller, Eberhard Lehmann, Anders Kaestner, Pierre Boillat, Tobias Panzner, and Uwe Filges. "Neutron radiography with sub-15μm resolution through event centroiding." Nuclear Instruments and Methods in Physics Research Section A: Accelerators, Spectrometers, Detectors and Associated Equipment 688 (2012): 32-40.

[49] Tremsin, A. S., J. B. McPhate, J. V. Vallerga, O. H. W. Siegmund, W. B. Feller, E. Lehmann, and M. Dawson. "Improved efficiency of high resolution thermal and cold neutron imaging." Nuclear Instruments and Methods in Physics Research Section A: Accelerators, Spectrometers, Detectors and Associated Equipment 628, no. 1 (2011): 415-418.

[50] Llopart, Xavier, Rafael Ballabriga, Michael Campbell, Lukas Tlustos, and Winnie Wong. "Timepix, a 65k programmable pixel readout chip for arrival time, energy and/or photon counting measurements." Nuclear Instruments and Methods in Physics Research Section A: Accelerators, Spectrometers, Detectors and Associated Equipment 581, no. 1 (2007): 485-494.

[51] Cremer, Christoph, and Thomas Cremer. "Considerations on a laser-scanning-microscope with high resolution and depth of field." Microscopica acta (1974): 31-44.

[52] STM E545-14, Standard Test Method for Determining Image Quality in Direct Thermal Neutron Radiographic Examination, ASTM International, West Conshohocken, PA, 2014, www.astm.org.

[53] Neitzel, Ulrich, Egbert Buhr, Gerhard Hilgers, and Paul R. Granfors. "Determination of the modulation transfer function using the edge method: influence of scattered radiation." Medical physics 31, no. 12 (2004): 3485-3491.

[54] S. C. Vogel, A. S. Losko, M. A. M. Bourke, K. J. McClellan, R. Fielding, "Neutron Characterization of Encapsulated Metallic Fuel", Report to DOE/NE, NTRD-FUEL-2017-000064 (2017).